RIGA TECHNICAL UNIVERSITY

Sergejs Beļuns

BIO-INSPIRED WOOD MIMIC MATERIALS CREATED BY RECOMBINING CELLULOSE, HEMICELLULOSE AND LIGNIN

Summary of the Doctoral Thesis

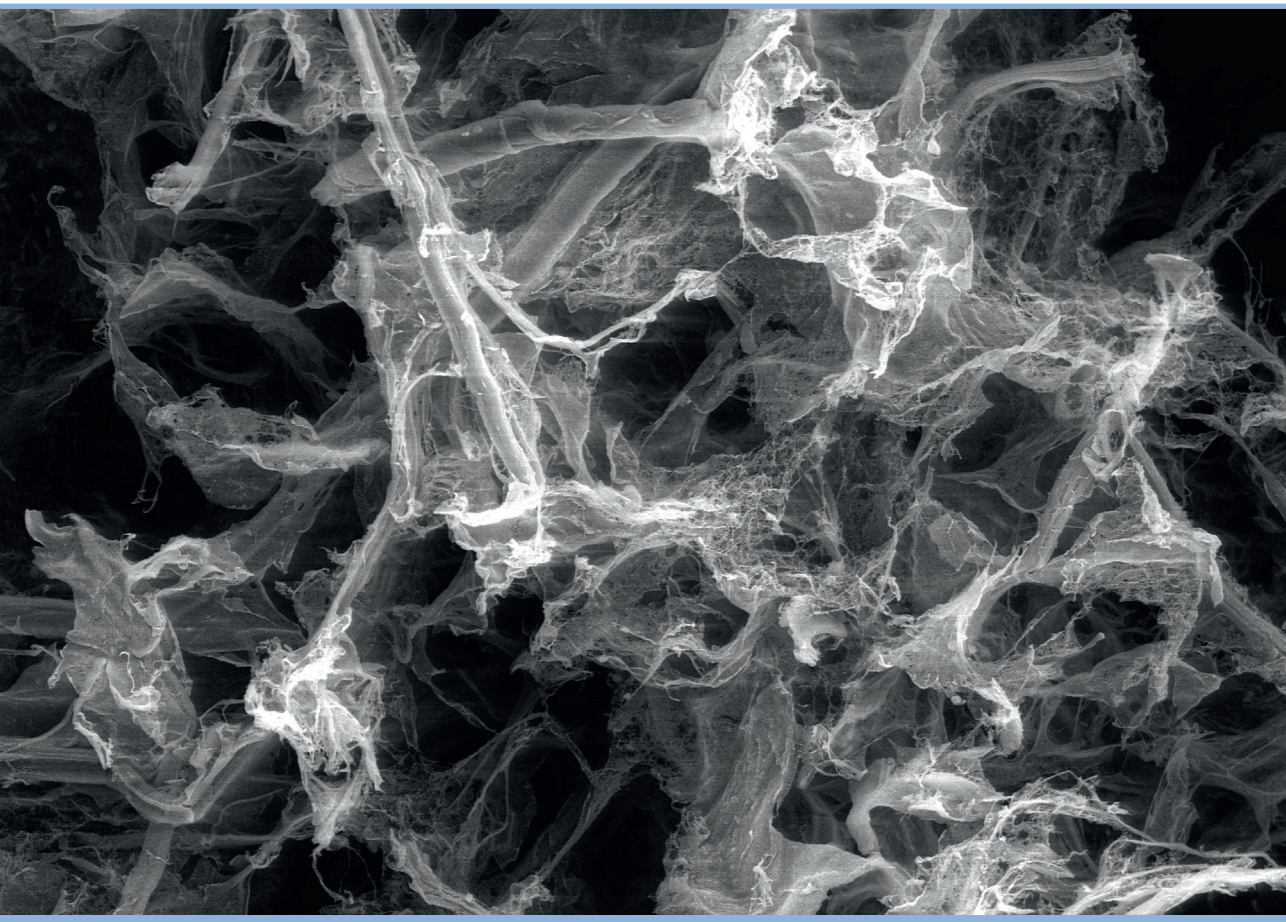

RTU Press
Riga 2024

RIGA TECHNICAL UNIVERSITY
Faculty of Natural Sciences and Technology
Institute of Chemistry and Chemical Technology

Sergejs Beļuns
Doctoral Student of the Study Programme "Chemistry, Materials Science and Engineering"

BIO-INSPIRED WOOD MIMIC MATERIALS CREATED BY RECOMBINING CELLULOSE, HEMICELLULOSE AND LIGNIN

Summary of the Doctoral Thesis

Scientific supervisors
Professor Dr. sc. ing.
SERGEJS GAIDUKOVS
Professor Ph. D.
VIJAY KUMAR THAKUR

RTU Press
Riga 2024

Beļuns, S. Bio-inspired Wood Mimic Materials Created by Recombining Cellulose, Hemicellulose and Lignin. Summary of the Doctoral Thesis. – Riga: RTU Press, 2024. 64 p.

Published in accordance with the decision of the Promotion Council "RTU P-02" of 19 February 2024, Minutes No. 04030-9.2.2/2.

Investigation, preparation, and testing of the materials was performed at the Institute of Chemistry and Chemical Technology of Riga Technical University.

This research was carried out within the scope of project RealHLC No. lzp-2019/1-0390, funded by the Latvian Council of Science.

This research has been supported by the Riga Technical University Doctoral Grant Programme and by the European Social Fund within Project No. 8.2.2.0/20/I/008, "Strengthening of PhD students and academic personnel of Riga Technical University and BA School of Business and Finance in the strategic fields of specialization" of the Specific Objective 8.2.2 "To Strengthen Academic Staff of Higher Education Institutions in Strategic Specialization Areas of the Operational Programme "Growth and Employment"".

Cover picture by Sergejs Beļuns

https://doi.org/10.7250/9789934370717
ISBN 978-9934-37-071-7 (pdf)

ACKNOWLEDGEMENTS

I wish to convey my heartfelt thanks to my family whose constant love, support, and patience have been the bedrock of my journey.

My profound appreciation goes to my supervisor Sergejs Gaidukovs for his unwavering guidance, encouragement, and patience he provided throughout this process. I also extend my genuine gratitude to all my colleagues whose involvement and contributions have been invaluable. My special thanks and gratitude to my dear friend Oskars Platnieks for moral support and guidance. Additionally, I extend my thanks to the reviewers for their insightful critiques, recommendations, and direction.

I am deeply grateful to the Institute of Chemistry and Chemical Technology (Polymer Materials) of Riga Technical University, and the Latvian Council of Science and the European Social Fund for all the opportunities provided to me during my doctoral studies.

"Pain was a fascinating horror."
/Aldous Huxley/

DOCTORAL THESIS PROPOSED TO RIGA TECHNICAL UNIVERSITY FOR PROMOTION TO THE SCIENTIFIC DEGREE OF DOCTOR OF SCIENCE

To be granted the scientific degree of Doctor of Science (Ph. D.), the present Doctoral Thesis has been submitted for defence at the open meeting of RTU Promotion Council on 10 June 2024, at 10.00 at the Faculty of Natural Sciences and Technology of Riga Technical University, Paula Valdena iela 7, Room 272.

OFFICIAL REVIEWERS

Dr. sc. ing. Jānis Rižikovs
Latvian State Institute of Wood Chemistry, Latvia

Associate Professor Dr. Eero Kontturi
Aalto University, Finland

Associate Professor Dr. Darshil U.Shah
University of Cambridge, United Kingdom

DECLARATION OF ACADEMIC INTEGRITY

I hereby declare that the Doctoral Thesis submitted for review to Riga Technical University for promotion to the scientific degree of Doctor of Science (Ph. D.) is my own. I confirm that this Doctoral Thesis has not been submitted to any other university for promotion to a scientific degree.

Sergejs Beļuns …….. (signature)

Date: ……

The Doctoral Thesis has been written in English. It consists of an Introduction, 3 chapters, Conclusions, 52 figures, and 15 tables; the total number of pages is 139. The Bibliography contains 240 titles.

TABLE OF CONTENTS

ABBREVIATIONS

CA	citric acid
CI	crystallinity index
CNF	cellulose nanofibers
CNP	cellulose nanopaper
DI	deionized water
FESEM	field emission scanning electron microscopy
FFD	full-factorial design
FTIR	Fourier Transform Infrared Spectroscopy
G	glycerol
H	hemp
L	lignin
NC	nanocellulose
NFC	nanofibrillated cellulose
NP	nanopaper
P	pectin
PEG	polyethylene glycol
RH	relative humidity
SEM	Scanning Electron Microscopy
STEM	Scanning Transmission Electron Microscopy
TGA	Thermogravimetric Analysis
WAXD	Wide angle X-ray diffraction
WM	wood mimic
wt%	weight percent
X	xylan

INTRODUCTION

Recent advancements in sustainable materials have significantly focused on composite materials using renewable biomass fibers, particularly cellulose. This biopolymer, derived from plant fibers, is recognized for its biodegradability, renewability, and suitability for nanoscale manufacturing. These attributes render it ideal for reinforced materials, providing high strength-to-weight ratios for diverse applications. Ongoing research into nanocomposites featuring nanocellulose has exhibited versatile potential, leading to the development of advanced materials for hybrid composites, films, and foams. Additionally, there is a growing interest in biomimetic materials, with wood-like composites made of cellulose, hemicellulose, and lignin attracting attention due to their environmental sustainability.

The Doctoral Thesis is centered on extracting and altering nanocellulose and nanolignocellulose from various biomass sources, including wood pulp, dust, and agricultural residues like hemp stalks. It should be noted that nanocellulose and nanolignocellulose differ only in the content of cellulose in nanofibers, which can be regulated by chemical treatment; and in the Thesis they will be denoted by the abbreviation NFC, which is an abbreviation of the widely used English term nanofibrillated cellulose (NFC). Process also involves utilizing external biopolymers like hemicellulose (xylan) and lignin. These biopolymers are then thoroughly combined in controlled ratios to create composites that emulate the structural and mechanical properties of natural wood. The research explores two key material preparation methodologies: creating wood mimic composite thin films (nanopapers) and developing lightweight foams. Both methods incorporate advanced techniques such as chemical modification, nanofibrillation, and blending with other biodegradable polymers, showcasing the innovative approaches in creating sustainable composite materials. The research can be divided into 4 main phases:

Phase 1: Developing nanopapers from nanocellulose, examining the effects of lignin and xylan as modifiers, and assessing how environmental factors like UV radiation and moisture affect cellulose nanopaper composites.

Phase 2: Developing sustainable bioplastics from hemp stalks, this phase involved creating adjustable properties through reversible thermal crosslinking of cellulose. A crosslinking blend with glycerol, xylan, citric acid, and polyethylene glycol (PEG) was used, allowing tunability in properties from brittle to ductile.

Phase 3: Lightweight foams were prepared from wood dust and hemp stalk waste. These foams, with a density range of 2–36 mg/cc, were analyzed for mechanical response, porosity, thermal conductivity, and morphology, indicating potential applications.

Phase 4: In the final phase, the research explores further functionalization and the creation of sustainable, multifunctional foams using hemp stalk waste and other materials like lignin, xylan, pectin, glycerol, and citric acid. These foams exhibited various microstructures, densities, high porosity, and absorption capacities, with some being hydrophobic and adaptable in structure, suitable for insulation, filtration, and environmental cleanup applications.

Aim of the Doctoral Thesis

The main aim is to prepare and investigate systematically advanced biopolymer materials using renewable raw materials of nanolignocellulose, hemicellulose, and lignin extracted from biomass waste through a strategy of their recombination and reassembly and also the introduction of additional green chemistry routes of components functionalization and cross-linking to adjust circularity and performance properties of the resulting wood-imitating materials such as films and foams.

Tasks of the Doctoral Thesis

1. To extract nanolignocellulose from different sources of biomass waste with the microfluidization method.
2. To develop green chemistry methods of nanolignocellulose functionalization with biopolymers and crosslinking to tune up the structure and properties of obtained bioplastics.
3. To develop nanolignocellulose papers, bioplastic films, and bio-foams (sponges) inspired by wood structures that can potentially replace fossil-based ones.
4. To validate the performance and structure relationship of obtained lignocellulosic bioplastic materials.

Thesis statements to be defended

1. Nanolignocellulose, extracted and manipulated from hemp and birch wood biomass, can be recombined with hemicellulose and lignin and processed into wood-mimicking biopolymer papers, films, and foams (sponges).
2. The structure of nanocellulose papers and bio-foams can be regulated by adjusting the content of lignin and hemicellulose, as well as by green chemical functionalization and physical crosslinking.
3. The varying ratios of xylan, lignin, and nanolignocellulose components, as well as the content of citric acid crosslinking agents and dicumyl peroxide initiator, can systematically fine-tune the performance, biodegradation, and circularity of the film bioplastics.
4. The bio-foams (sponges) show tuneable structures ranging from soft to rigid behavior and their applicability in thermal insulation, filtration systems, and environmental cleanup, among other potential uses.

Scientific novelty

The novel wood-mimicking lignocellulose contains biopolymer materials such as foams, films, and paper with regulated structure and adjustable performance properties. The developed

100 % biomaterials have very wide applications in the production of various packaging, coatings, sorbents, and building materials to replace fossil-origin plastics.

Practical significance

1. Transforming waste from agriculture and paper waste (with pretreatment) materials into valuable composites demonstrates a sustainable approach to resource utilization.
2. Developing wood-like composites can produce lighter, high-performance materials for use across various industries.
3. Adjustable hemp-based bioplastics create a flexible, eco-friendly alternative to traditional plastics.
4. The production of lignocellulose foams offers a green substitute for conventional insulating or packaging materials.

Approbation of the PhD Thesis in Scopus and Web of Science indexed articles

Literature review

1. Platnieks, O., **Beluns, S.**, Briede, S., Jurinovs, M., Gaidukovs, S. Cellulose synergetic interactions with biopolymers: Functionalization for sustainable and green material design (2023), Industrial Crops and Products, 204, 117310. DOI: 10.1016/j.indcrop.2023.117310.
   Chapter 3.1.
2. **Beluns, S.**, Gaidukovs, S., Platnieks, O., Barkane, A., Gaidukova, G., Grase, L., Nabels-Sneiders, M., Kovalovs, A., Thakur, V. K. Clean manufacturing of cellulose nanopapers by incorporating lignin and xylan as sustainable additives (2022), Carbohydrate Polymer Technologies and Applications, 3, 00207. DOI: 10.1016/j.carpta.2022.100207.
   Chapter 3.2.
3. **Beluns, S.**, Platnieks, O., Gaidukovs, S., Starkova, O., Sabalina, A., Grase, L., Thakur, V. K., Gaidukova, G. Lignin and xylan as interface engineering additives for improved environmental durability of sustainable cellulose nanopapers (2021), International Journal of Molecular Sciences, 22 (23), 2939**.** DOI: 10.3390/ijms222312939.
   Chapter 3.3.
4. **Beluns, S.**, Gaidukovs, S., Platnieks, O., Grase, L., Gaidukova, G., Thakur, V. K. Sustainable hemp-based bioplastics with tunable properties via reversible thermal crosslinking of cellulose (2023), International Journal of Biological Macromolecules, 242, 125055. DOI: 10.1016/j.ijbiomac.2023.125055.
   Chapter 3.4.
5. **Beluns, S.**, Gaidukovs, S., Platnieks, O., Gaidukova, G., Mierina, I., Grase, L., Starkova, O., Brazdausks, P., Thakur, V.K. From wood and hemp biomass wastes to sustainable nanocellulose foams (2021), Industrial Crops and Products, 170, 113780. DOI: 10.1016/j.indcrop.2021.113780.

Chapter 3.5.

6. **Beluns, S.,** Platnieks, O., Jurinovs, M., Buss, R., Gaidukovs, S., Orlova, L., Starkova, O., Thakur, V.K. Sustainable Foams from Hemp, Lignin, Xylan, Pectin, and Glycerol: Tunable via Reversible Citric Acid Crosslinking for Absorption and Insulation Applications (2024), Giant, **(accepted)**.

Other publications on the topic that are not included in the Thesis

1. **Beluns, S.**, Platnieks, O., Sevcenko, J., Jure, M., Gaidukova, G., Grase, L., Gaidukovs, S. Sustainable Wax Coatings Made from Pine Needle Extraction Waste for Nanopaper Hydrophobization (2022), Membranes, 12 (5), 537. DOI: 10.3390/membranes12050537.
2. Budtova, T., Aguilera, D.A., **Beluns, S.**, Berglund, L., Chartier, C., Espinosa, E., Gaidukovs, S., Klimek-kopyra, A., Kmita, A., Lachowicz, D., Liebner, F., Platnieks, O., Rodríguez, A., Navarro, L. K. T., Zou, F., Buwalda, S. J. Biorefinery approach for aerogels (2020), Polymers, 12 (12), 2779, pp. 1-63. DOI: 10.3390/polym12122779.

Presentations at international scientific conferences

1. **Beluns, S.**, Gaidukovs, S. Lignocellulose based aerogel preparation from wood and hemp waste materials. In: RTU 61st International Scientific Conference, Materials Science and Applied Chemistry 2020. Latvia, Riga, October 23, 2020. Online, Oral presentation.
2. **Beluns, S.**, Gaidukovs, S. Biobased low density and high porosity lignocellulose composite materials from wood and hemp waste. Functional Materials and Nanotechnologies FM&NT-2020. Lithuania, Vilnius, November 23–26, 2020. Online, Poster.
3. **Beluns, S.**, Gaidukovs, S. Xylan/Lignin modified biocomposites from lignocellulose waste. 1st Greenering international conference. Portugal, Costa da Caparica, February 15–16, 2021. Online, Poster.
4. **Beluns, S.**, Gaidukovs, S. Sustainable ultralight and completely biobased lignocellulose foams from waste cellulosic nanomaterials. Training school "Advanced Technologies for the processing and characterization of nanostructured materials". July 5–6, 2021. Online, Oral presentation.
5. **Beluns, S.**, Gaidukovs, S. Sustainable ultralight foams from wood and hemp waste cellulosic nanomaterials for thermal insulation applications. Conference: Aerogel Industry-Academia Forum. July 13–15, 2021. Online, Poster.
6. **Beluns, S.**, Gaidukovs, S. Biobased lignocellulose composite cryogels from hemp waste. 7th International Polysaccharide Conference. France, Nantes, October 11–15, 2021. Poster.
7. **Beluns, S.**, Gaidukovs, S., Platnieks, O., Barkane, A. Lignin and Xylan addition to cellulose nanopaper – a sustainable solution to improve properties. In: RTU 62nd

International Scientific Conference "Materials Science and Applied Chemistry 2021". Latvia, Riga, October 22, 2021. Online, Oral presentation.

8. **Beluns, S.**, Gaidukovs, S. From hemp stalk waste to porous wood-mimic foams. 5th EPNOE Junior Scientist Meeting 2022. Portugal, Aveiro, September 8–9, 2022. Poster.
9. **Beluns, S.**, Gaidukovs, S. Ultralightweight biobased foams from hemp stalk waste with tunable mechanical properties and shape recovery effect. 7th International Conference on Multifunctional, Hybrid and Nanomaterials. Italy, Girona, October 19–22, 2022. Poster.
10. **Beluns, S.**, Gaidukovs, S., Paltnieks, O. Thermally crosslinked hemp-based cellulose bioplastics with tunable properties and reversible reaction. Nordic Polymer Days 2023. Denmark, Kopenhagen, May 8–10, 2023. Poster.
11. **Beluns, S.**, Gaidukovs, S., Paltnieks, O. Thermally crosslinked cellulose bioplastics derived from hemp with tunable properties and reversible reaction. Renewable Resources & Biorefineries RRB 2023. Latvia, Riga, May 31 – June 2, 2023. Poster.
12. **Beluns, S.**, Gaidukovs, S. Wood mimic composites from cellulose, hemicellulose and lignin. In: RTU 64th International Scientific Conference “Materials Science and Applied Chemistry 2023”. Latvia, Riga, October 6, 2023. Oral presentation.

1. LITERATURE REVIEW

1.1. Sustainable synergies: the role of biopolymers in functional material innovation

Biopolymers are slowly transitioning to become the critical raw materials of the modern economy [1,2]. This occurs as we approach the inevitable limits of fossil resources and tackle the reliance built upon them. Resource and energy production efficiency are two significant issues facing the global economy. This marks the modern approach, i.e., extracting more value from waste and byproducts and the formation of efficient recycling routes as means to recover energy and time inputs used in biological and chemical production systems [2,3]. In addition, half a century of extensive use of fossil-based polymers has left a tremendous amount of non-biodegradable pollution. In contrast, extensive use of chemical processing has led to toxic chemicals accumulating in the environment [4]. For these reasons and more, biopolymers, as a renewable, non-toxic, and biodegradable source of materials, have become the focus of modern material science and chemical engineering. Recent trends in various materials like hydrogels [5,6], aerogels [7,8], films [9,10], and fibers [11,12] show an increasing number of works focused on biopolymer-centered systems.

The abundant natural biopolymers can be divided into three large groups: polysaccharides, polyphenols, and proteins. The availability of various crop polysaccharides and lignin as the most prominent representative of polyphenols has seen an increasing number of researchers exploring these relatively cheap and renewable biomass wastes [13]. The transformation of raw material harvesting requires approaching the crops as multipurpose plants where every section sees the application. Similarly, the isolated material concept has been slowly phased out with the requirement for more advanced functional materials. More research has been dedicated to bottom-up processes and understanding various biopolymer roles and their synergetic interactions in living organisms [14]. This approach coincides with the rapidly growing popularity of bacterial cellulose and nanocellulose applications in material preparation [15,16]. Biopolymers are more complex than their synthetic counterparts. Still, with advancements in the computing power of modeling, nanotechnology, and even artificial intelligence, our understanding of molecular interactions and hierarchical assembly is growing rapidly. Studies that analyze biopolymer interfacial interactions [17] and create optimal routes for assembly methods of biopolymer networks [18] are increasing annually.

1.2. Processing biopolymers into functional materials

The design and integration of biopolymers into various materials must consider biopolymer characteristics. Biopolymers form strong intermolecular bonds, start to degrade at relatively low temperatures, and are often challenging to dissolve in large quantities. Thus, classical thermoplastic processing is not a suitable method for preparing biopolymer materials, although some workarounds that mimic these plastic properties are known, e.g., thermoplastic starch. In the case of solvents, there are often tradeoffs between quality, efficiency, price, and toxicity.

Greener cellulose dissolving options, like an alkali/urea solution, have recently become popular [19-21]. Similarly, options like ionic liquids and deep eutectic solvents are widely explored [22-24].

Research with materials prepared from biopolymer suspensions often shows mechanical and morphological properties comparable to those of the dissolved cellulose approach, especially if nanoparticle suspensions are used [25]. Using biopolymer suspensions with water as a liquid medium is generally desirable as a green, cheap, and non-toxic route. Water that does not dissolve but swells biopolymers due to physically crosslinked polymer networks can be considered an advantage. Chemical crosslinking is commonly used to control the final structure for tuned properties [26]. These crosslinked water-swelled networks, often known as hydrogels, have seen massive interest in the biomedical research field but are not limited to other applications like sorbents for water treatments, sensors, stimuli-responsive devices, and others [27,28]. Aerogels or foams, which frequently start in the form of gels or hydrogels, are a particular class of adaptable, lightweight, high-specific-surface-area, and low thermal conductivity materials [29]. Aerogel powder can be employed as a drug delivery agent, while typical applications include thermal or sound insulation, sorption, catalyst carriers, sensors, stimuli-responsive devices, and others [30,31].

Fibers are a crucial material type gradually returning to their bio-based and biodegradable origins. The return to biopolymer-based fibers aims to create biocompatible and biodegradable composites. Fibers obtained from renewable sources aim to counter fossil polymer pollution and non-renewable and energy-demanding processes applied to produce widely used glass and carbon fibers [32]. Similarly, versatile and biodegradable polymer films could replace fossil-based plastic packaging. This is especially important since packaging and one-time-use plastic products often end up in the wrong waste streams, are hard to recycle, and contribute to growing landfills [33]. Nevertheless, biopolymer films are not limited to such applications and can be applied to modern electroconductive materials, tissue recovery, skin impedance sensors, and other applications [34].

Biopolymer materials are extensively studied in biomedical fields due to their high value-added applications and biocompatibility, e.g., hydrogel consistency and water uptake can mimic living tissue [35]. Biopolymer fiber mats and films serve as excellent scaffolds for tissue recovery [36,37]. All forms of biopolymer materials have been used in some way or another to deliver active drug compounds [38,39]. While these are just some examples of biomedical applications, the main potential and growth of the biopolymer material field are centered around the industries widely dominated by conventional polymers and composites, such as adhesives, automotive, electronics, packaging, construction, etc.

2. MATERIALS AND METHODS

2.1. Materials

Cellulose and lignocellulose source

High-purity cellulose was obtained from old, unutilized laboratory filter paper. Paper was shredded using Retsch SM300, with a sieve size of 2.00 mm. The process was repeated with a sieve size of 0.25 mm, and for both pass-throughs, the mill rotation speed was 1500 rpm. The milled paper was used without further purification and treatment.

As the first processing waste, dried Santhica 27 variety hemp stalks were collected from a private farm in Latvia. The Retsch cutting mill SM300 (Retsch GmgH, Haan, Germany) was used to grind hemp stalks. The first grinding cycle used a sieve size of 4.00 mm, followed by the second and third milling cycles, which used sieve sizes of 0.25 mm and 0.12 mm, respectively. The mill was manually fed, and the rotation speed was set to 1500 rpm throughout the process.

Wood dust flour was obtained from Latvian birch plywood producer "Latvijas finieris" JSC as industrial waste from the plywood sanding process and was used as received.

Other chemicals

Laboratory-grade sodium hydroxide (NaOH) was used for lignin suspension preparation without further purification. Kraft lignin was purchased from Merck KGaA (Darmstadt, Germany) and used as received without additional processing. Beechwood xylan was purchased from Carl Roth GmbH (Karlsruhe, Germany). Merck KGaA (Darmstadt, Germany) provided PEG 300 (polyethylene glycol), apple pectin, glycerol, citric acid (CA), tert-butanol and dicumyl peroxide. All processes and sample preparation were carried out with deionized (DI) water.

Nanofibrillated cellulose and lignocellulose

For nanopaper production, nanofibrillated cellulose (NFC) and nanofibrillated lignocellulose were prepared by dispersing 1 wt% of milled paper or milled hemp in DI water. Both nanofibrillated celluloses are hereafter abbreviated as NFC or NC (nanocellulose). The obtained aqueous dispersion was mixed in an ordinary kitchen blender (800 W) and then passed through a microfluidizer (LM20, Microfluidic, U.S.A.) equipped with a chamber H210Z (200 μm). Five passes were used to increase the degree of defibrillation. The pump pressure was set at 30,000 psi.

For lignocellulose foam production, alkaline treatment was used to remove lignin, hemicellulose, and other non-cellulosic substances from source waste material to facilitate the mechanical defibrillation process. Separately, wood and hemp were immersed into 5 wt% NaOH solution (cellulose to NaOH solution ratio was 1:8) in the stainless-steel kettle and heated up to 80 °C for 3 h under continuous stirring. Afterwards, the solution was carefully discarded, replaced with a fresh one, and left overnight at room temperature under constant stirring. After treatment, wood and hemp particles were filtered and washed with DI water until the slurry's pH reached DI water values (around 7.0). The obtained slurry was dried in a laboratory oven at

50 °C. Hemp showed around 68 % and 89 % cellulose content, while for wood samples – around 40 % and 57 % before and after treatment, correspondingly [61].

Nanolignocellulose suspensions with concentrations of 0.2 wt%, 0.5 wt%, and 1.0 wt% were prepared from alkaline treated wood and hemp waste powders by redispersing them in DI water with vigorous stirring for 8 hours. The obtained aqueous suspensions were passed through a microfluidizer (LM20, Microfluidic, U.S.A.) with chamber H210Z (200 μm), as described previously. High cellulose concentration dispersions clog the apparatus, so the 3.0 wt% was obtained from 1.0 wt% suspension by evaporating excess water at 80 °C with continuous stirring until the desired concentration was achieved.

For the Phase 4 study, an aqueous suspension containing 1.5 wt% of the ground hemp (without chemical treatment) was prepared using deionized water. This suspension was mixed in a conventional 800 W kitchen blender for 2 minutes, then processed in a Microfluidics microfluidizer. The microfluidizer was set to a pressure of 30,000 psi, and the material underwent five passthrough cycles for uniform defibrillation. The process resulted in the production of hemp NFC with dimensions of 86 ± 41 nm.

Lignin and xylan solution preparation

50 g of kraft lignin was first suspended in 470 mL of DI water and stirred magnetically for 1 h at 85 °C. The suspension was stabilized to pH 10 using a strong alkaline solution (NaOH). A dark, homogeneous suspension was obtained, having a lignin concentration of 10 wt% (adjusted with evaporation). For the Phase 4 study, this suspension was then passed through medium-pore laboratory filter paper using a Büchner funnel, a Bunsen flask, and a vacuum pump system. A second filtration was conducted using smaller pore-sized filter paper. After these steps, the final lignin solution had a concentration of 2.2 wt%.

30 g of beechwood xylan was dissolved in 285 mL of DI water and stirred magnetically at 80–85 °C for 1 h until the xylan dissolved in the water. A slightly brown, viscous solution was obtained, having a xylan concentration of 10 wt% (adjusted with evaporation). After cooling at room temperature, both solutions were used in the preparation of the samples.

Cellulose and lignocellulose nanopaper preparation

Nanopaper films from wastepaper were produced by casting 1 wt% NFC dispersion onto polystyrene Petri dishes. Dispersions and solutions were mixed (with xylan and lignin) to selected concentrations, magnetically stirred for 2 h, cast onto prepared Petri dishes, and placed at room temperature until evaporation. Afterwards, the nanopaper films were dried in a laboratory oven at 50 °C for 24 h. 1 wt%, 2.5 wt%, 5 wt%, 10 wt%, 20 wt%, and 30 wt% of lignin (L) and xylan (X) loadings into cellulose nanopaper were prepared. In the text, single filler samples have been abbreviated as L and X, combined with the filler concentration number. At the same time, several complex compositions with simultaneous lignin and xylan loading were also proposed, abbreviated as LX systems. For example, the X1 sample corresponds to xylan 1 wt% loading, L1 sample – lignin 1 wt% loading, L1X1 sample – lignin 1 wt% and xylan 1 wt% complex loadings. A sample without any loading is abbreviated as cellulose nanopaper (CNP).

Hemp paper films were made by pouring a microfluidized 1 wt% dispersion onto 145 mm polystyrene (PS) Petri plates and leaving them at room temperature until evaporation. The films were then dried in a laboratory oven at 50 °C for 24 h.

Hemp paper impregnation – preparation of bioplastics

A 10 wt% xylan solution was combined with PEG, glycerol, and citric acid in various weight ratios. To better facilitate and catalyze the crosslinking reaction, dicumyl peroxide was also added (0.1 wt% of the mixture's total weight dissolved in roughly 1–2 ml of acetone). The combined mixture was stirred until the citric acid was completely dissolved and the mixture was homogeneous. The prepared mixture was poured into a polystyrene petri dish, and the previously prepared hemp paper was fully immersed in the mixture overnight. Before temperature treatment, any excess mixture was gently scraped off the paper, leaving only impregnated paper. The impregnated paper was then crosslinked in a laboratory oven for 12 h at 140 °C. The names of the prepared samples were derived from the weight ratios of the components, which were abbreviated as XPGC (X – xylan solution 10 wt%; P – PEG 300; G – Glycerol; C – Citric acid). For example, 2:1:2:2 is made up of two parts of xylan solution, one part of PEG 300, two parts of glycerol, and two parts of citric acid. Visual images of bioplastics and impregnated mixtures are shown in Fig. 2.1. Abbreviations throughout the work are used for impregnated hemp papers after 48 hours of washing in water and following the drying step unless specified otherwise. Hemp paper is abbreviated as “hemp,” and its structure is studied after initial paper casting.

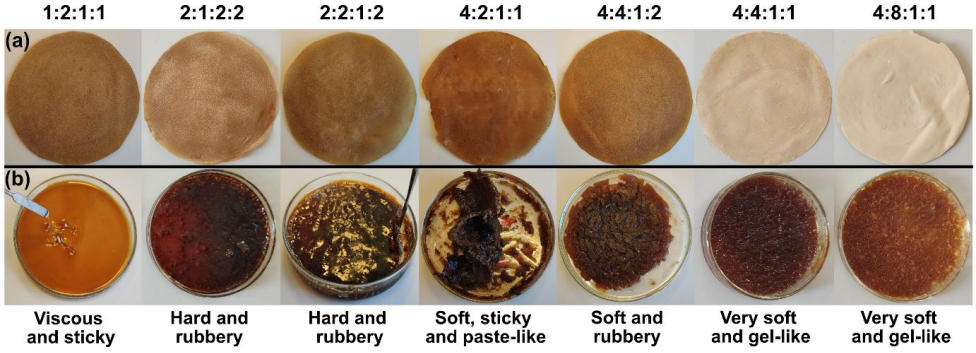

Fig. 2.1. (a) Hemp bioplastics after impregnation and crosslinking, (b) crosslinked impregnation mixture.

Nanolignocellulose foam preparation

Foams for the Phase 3 study were fabricated using the freeze-drying method. The obtained NC suspensions were vigorously stirred and poured into cylindrical polypropylene molds 35 mm in diameter. Afterwards, every mold was plunged into liquid nitrogen to freeze and solidify. Freeze-drying was done via a vacuum freeze dryer Sentry 2.0, VirTis SP Scientific, at a condenser temperature of –60 °C and a high vacuum of 200 mT. The sublimation process was carried out for 72 hours. The obtained foam samples were self-standing, lightweight, and soft.

For the Phase 4 study, crosslinked lignocellulose foams were prepared utilizing the freeze-drying technique according to the following detailed protocol. To produce unaltered lignocellulose foams, a 1.5 wt% hemp NFC suspension was combined with varying quantities of citric acid (CA), ranging from 0.5 g to 5 g per 100 g of suspension, corresponding to approximately 0.5–5 wt% CA. This mixture was vigorously agitated using a magnetic stirrer. To each blend, 10 wt% tert-butanol was added and similarly stirred vigorously. The resultant suspension was then transferred into cylindrical polypropylene trays with a diameter of 43 mm. These trays were subjected to freezing at –80 °C in the condenser chamber of a Telstar LyoQuest -85 plus freeze-dryer until they were completely solidified. Subsequently, the samples were relocated to the vacuum chamber of the freeze-dryer and subjected to a high vacuum of 0.03 mbar. The sublimation process was conducted over a period of 72 hours. The resulting foam samples were self-supporting, lightweight, and soft.

Thermal heating was employed to initiate the CA crosslinking reaction. Dicumyl peroxide (DP) was utilized as a catalyst for this reaction. A minuscule quantity of DP, specifically two flakes, was dissolved in 2 ml of acetone. This solution was then applied to the surface of the foam samples using a dropper, administering three drops per sample. Subsequently, the samples were placed in a laboratory oven at 140 °C for 6 hours to facilitate the crosslinking reaction. A pure hemp foam sample without added CA or crosslinking was also prepared for comparative purposes. The nomenclature for these samples was designated as H- (indicating hemp) and CA(0.5-5) to denote the amount of citric acid used. For example, H-CA0.5 refers to a hemp foam crosslinked with 0.5 g of CA.

For the creation of wood mimic (WM) foams, lignin and xylan solutions were incorporated into the same 1.5 wt% hemp NFC suspension to achieve a composition mimicking that of average hardwood: 45 % hemp, 35 % xylan and 20 % lignin by dry weight. The NFC suspension was thoroughly mixed with the lignin and xylan solutions using a magnetic mixer for 30 minutes. As in the previous process, similar quantities of citric acid and tert-butanol were added to the WM suspension and vigorously stirred. The subsequent steps for foam preparation were identical to those described earlier. A pure WM foam sample without added CA and crosslinking was also prepared for reference. The sample naming convention was analogous to the previous series, denoted as WM- (wood mimic) and -CA(0.5-5) for the quantity of citric acid added.

Furthermore, both hemp and WM suspensions were modified with pectin and glycerol. Compositions, including solely pectin or glycerol, as well as hybrid variants with both additives, were explored. For pectin-modified foams, varying amounts of pectin (0.25–1 g) were dissolved in the hemp NFC and WM suspensions and stirred magnetically at 80–85 °C for 1 hour until fully dissolved. Subsequently, 1 g of citric acid and 10 wt% tert-butanol were added. For the glycerol-modified versions, different glycerol quantities (0.5–2 g) were incorporated and similarly stirred. In both pectin and glycerol-modified foams, a constant amount of 1 g CA was used, with varying amounts of pectin and glycerol. The preparation steps for these foams were consistent with those outlined above. The sample naming scheme remained the same, with pectin denoted as -P and glycerol as -G. The amount of each component added is indicated next to the respective abbreviation. For instance, the hybrid

sample WM-P0.5-G2-CA1 comprises WM suspension, 0.5 g of pectin, 2 g of glycerol, and 1 g of citric acid. Overall, the schematic showing the main steps of foam preparation and some sample pictures are illustrated in Fig. 2.2.

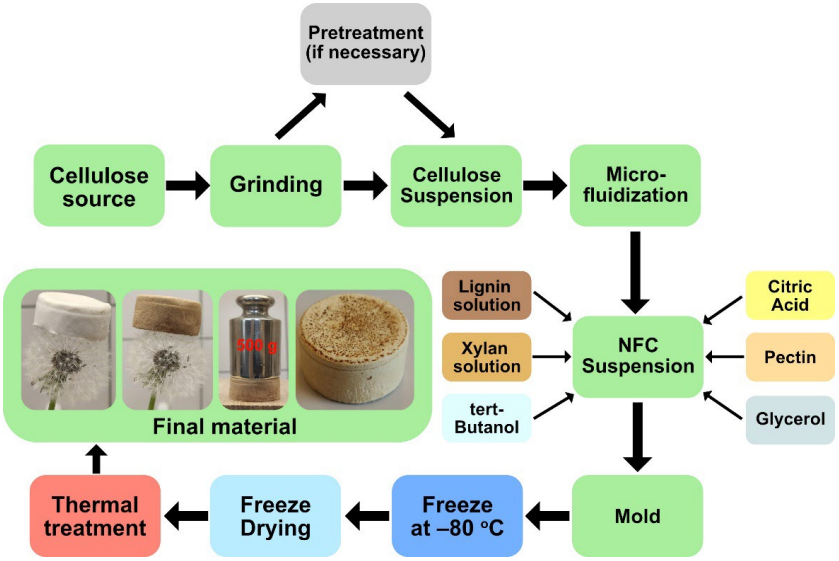

Fig. 2.2. Overall schematic showing the main steps of foam preparation and some sample pictures.

2.2. Testing methods

Zeta potential measurements

Zeta potential assessment of colloidal stability of prepared suspensions was acquired using a Malvern Zetasizer Nano ZS particle analyzer. Each defibrillated suspension was diluted with DI water to 0.01 wt%, sonicated for 5 min, and then analyzed. Measurements were made at ambient room temperature of 22 °C and pH of 7. Smoluchowski's model was chosen for the calculation of zeta potential. No additional electrolytes were added to the suspension.

Density, porosity, volume shrinkage

The apparent density of bioplastic and foam samples was calculated by dividing the weight of the sample by its volume. The sample's weight was measured by an analytical balance (readability 0.0001 g, Precisa XT 220A, Precisa Gravimetrics AG, Switzerland), and a digital caliper measured the dimensions of the sample at five different positions.

Porosity (P) was calculated by considering a simple mixing rule with a negligible gas density and using the apparent density (ρ_a) and the theoretical density (ρ_t) of the sample using Expression (2.1):

$$P(\%) = \left(1 - \frac{\rho_a}{\rho_t}\right) \times 100. \quad (2.1)$$

The theoretical density (ρ_t) of the sample was calculated using a simple density addition approach with Expression (2.2):

$$\rho_t = a\rho_{hemp} + b\rho_{XPGC}, \quad (2.2)$$

where *a* and *b* are percentile contributions in the sample; ρ_{hemp} is the skeletal density of cellulose (1.5 g/cm^3); and ρ_{XPGC} is the theoretical density of the impregnation mixture, which was also calculated using the same approach by adding each component density and its percentile contribution.

Volume shrinkage was determined by accurately measuring the dimensions (diameter and height) of the samples using a digital caliper with a precision of 0.01 mm. The calculation of percentage volume shrinkage was conducted using Expression (2.3).

$$Volume\ shrinkage(\%) = \frac{(V_m - V_s)}{V_m} \times 100, \quad (2.3)$$

where V_m and V_s are the volumes of the mold and sample after drying, respectively.

Sol content and water uptake

The unreacted part of the XPGC mixture that dissolves in water and can occur after the crosslinking reaction is referred to as the sol content. The sol content was determined by dissolving bioplastic in water for 48 h at room temperature with occasional stirring. After water treatment, the samples were dried in a laboratory oven at 60 °C until a consistent dried weight was achieved. The unreacted part of the XPGC mixture was calculated as the sol content using Expression (2.4):

$$Sol\ content(wt\%) = \frac{(m_0 - m_{dry})}{m_0} \times 100, \quad (2.4)$$

where m_0 is the initial sample weight and m_{dry} is the dry sample weight after rinsing with water.

Water uptake was determined similarly. Dry bioplastics were immersed in water at room temperature for 30 days after being treated with water. During this time, the sample weight was monitored; however, weight equilibrium was consistent after the first 24 hours. Samples were gently wiped with a paper towel before weighing. Water uptake was calculated using Expression (2.5):

$$Water\ uptake(\%) = \frac{(m_{wet} - m_0)}{m_0} \times 100, \quad (2.5)$$

where m_{wet} is the wet sample weight and m_0 is the initial sample weight.

Absorption capacity

The absorption capacity of foam samples was evaluated in various mediums, including water, rapeseed oil, and kerosene. Each sample was submerged in the respective medium for a duration of 5 minutes. The absorption capacity was quantitatively determined using Equation (2.6):

$$Absorption\ capacity(g/g) = \frac{(m_2 - m_1)}{m_1}, \quad (2.6)$$

where m_1 and m_2 are the foam weights before and after the immersion, respectively. Additionally, the cycling performance of the samples was assessed for water and kerosene

absorption (oil samples only lasted one cycle). This involved a systematic process where, after each absorption cycle, the sample was compressed to expel the absorbed fluid and then re-immersed in the medium for subsequent absorption measurements. This process was repeated until the sample either deteriorated or completed 10 cycles. For certain hydrophobic foam compositions, the absorption process in the water medium was further enhanced by mechanically compressing the sample.

Morphology

Particle size for raw wood and hemp waste particles was calculated using images from fibers deposited on a glass slide taken using an optical microscope Leica DMR (Leica Microsystems, Germany) at 10x magnification. Leica Image Suite™ software was used for measuring fiber length and diameter. A hundred measurements were acquired, and statistical analyses were performed to identify mean fibers such as particle length and diameter.

The FEI Nova NanoSEM 650 Schottky field emission scanning electron microscope (FESEM) was used to examine the morphology and structure of prepared materials. The morphology of nanopapers and bioplastics was studied with Scanning Electron Microscopy (SEM) at a voltage of 10 kV. Crosscuts were obtained in liquid nitrogen. Coatings were not applied on the surface or crosscut surfaces. Phase 4 foam samples, prior to the examination, were coated with a 3.6 nm layer of gold.

To acquire images of NFC, a Scanning Transmission Electron Microscopy (STEM) probe was used. Measurements were performed in transmission configuration using an acceleration voltage of 10 kV. A 400 W ultrasound probe was used to sonicate a diluted NFC suspension for 1 minute. After that, the NFC suspension droplet was placed on a copper grid (mesh 200) and allowed to evaporate at room temperature.

Thermal characterization

The thermal stability was evaluated with thermogravimetric analysis (TGA) using a Mettler TG50 instrument. Measurements were performed on samples with a weight of about 10 mg. Heating under an oxygen atmosphere was conducted from 25 °C to 750 °C with a heating rate of 10 °C/min.

The thermal conductivity and thermal diffusivity were evaluated with the Netzch LFA 447 NanoFlash System. The film specimens were heated with a Xenon flash lamp (10 J/pulse) in the air. The measurements were taken at three temperatures: 25 °C, 35 °C, and 45 °C. Before testing, the samples were coated with graphite to enhance the absorption of light energy and the emission of infrared radiation to the detector.

The thermal conductivity of foams was determined by the transient plane source method HotDisk TPS500. A sensor with a radius of 3.189 mm was placed between two identical cylindrical samples with a diameter of 30 mm and a total height (distance) of more than 10 mm. 10 mW power was supplied to the sensor, and a measurement time was set to 20 s. These parameters were experimentally found as optimal ones to satisfy requirements for the device and material type, i.e., allowable ranges for the characteristic time, probing depth, and temperature increase. For each pair of samples, five measurements were repeated with 15-

minute intervals between them. The thermal conductivity (k) was calculated using at least three intervals from temperature vs. time curves. The mean values for k are average from at least fifteen measurements. The effective thermal conductivity is expressed as a sum of two components (2.7):

$$k = k_c + k_r, \tag{2.7}$$

where k_c is a combination of thermal conductivity from gas and solid, and k_r is a combination of the radiation through the skeleton and contribution from voids. Four models are considered to calculate the effective thermal conductivity of the produced foams.

UV irradiation

Samples with thicknesses around 0.1 mm in the shape of strips, 10 mm in width and 40 mm in length, were cut from films. Before testing, samples were stored in a thermostat at 50 °C and RH < 10 %. These samples are considered dry reference samples. The samples were removed from the thermostat (50 °C and RH < 10 %). Films were irradiated with 1.6 W/cm^2 intensity and at a fixed distance of 25 cm from the source. A deep UV exposure lamp (Hg, 1000 W) with a broad emission spectral range from 200 nm to 600 nm was used as an irradiation source in an air environment. The constant temperature of 80 °C was maintained in the experimental chamber with the UV lamp. Exposure time was set to 6 h, 12 h and 24 h. After irradiation, samples were collected in sealable plastic bags and kept for 24 h, before performing a tensile test.

X-ray diffraction (XRD)

The wide-angle X-ray diffraction (WAXD) measurements were carried out to evaluate the crystallinity of the NC. They were obtained on a Panalitical X'Pert PRO diffractometer at a temperature of 20 °C. The monochromatic irradiation of CuKα with a wavelength of λ = 0.154 nm in the range of scattered radiation angles 2θ from 5° to 40° was used. The voltage was 40 kV, the current was 30 mA, and the scanning rate was 0.05 deg/s. The crystallinity index (CI) was calculated using the empirical equation (2.8) by Segal et al. method [40,41]:

$$CI(\%) = \left(1 - \frac{I_{am}}{I_{002}}\right) \times 100, \tag{2.8}$$

where I_{002} is the maximum intensity of the lattice's diffraction band located in the interval 2θ = 21–23°. I_{am} is the minimum intensity for diffraction band 2θ = 18–20°, which corresponds to an amorphous part.

Spectroscopy

Nicolet 6700 (Thermo-Scientific, Waltham, MA, USA) Fourier transform infrared spectroscopy (FTIR) in attenuated total reflectance (ATR) mode was used to investigate prepared material with a resolution of 4 cm^{-1} in the 650–4000 cm^{-1} range. Sixteen measurements were made on each specimen, and the average spectrum was given.

Rheology

Rheological measurements were recorded using an Anton Paar Smart Pave 102 (Graz, Austria) rheometer with a parallel plate measuring system PP25 (plate diameter 25 mm). The

crosslinking reaction was monitored using a time sweep measurement at a constant temperature of 140 °C. Time sweep measurements were carried out with a strain of 0.2 % and a frequency of 3 Hz. The initial gap was set to 0.3 mm with no force adjustment. These parameters were chosen to mimic the stationary crosslinking process and are in the linear viscoelastic region (LVR), as determined by a strain sweep experiment.

Moisture absorption

Samples were conditioned in desiccators under different relative humidity environments (RH %) at a room temperature of 22 °C. The humid environments were created by using different saturated salt solutions: $KC_2H_3O_2$ (RH24 %), NaCl (RH75 %), and K_2SO_4 (RH97 %). Gravimetric measurements were made with an accuracy of 0.01 mg, and the relative weight changes of samples w [%] were determined as weight gain per weight unit. Moisture saturation was achieved within 3–7 days. Retention of the mechanical properties after moisture desorption was studied on samples initially saturated at RH75 % and RH97 % and then conditioned at RH24 % until weight stabilization: abbreviated as RH75-->24 % and RH97-->24 %, respectively.

Hydrophobicity

The water contact angle (WCA) was measured using the static sessile drop technique, employing a Theta Lite optical tensiometer (Attension® Biolin Scientific, Gothenburg, Sweden). This process involved making five distinct measurements for 60 seconds, each using a 2 µL droplet of water placed on the surface of the specimen.

Mechanical properties

Tensile tests were performed on nanopaper films using a universal testing machine, Tinius Olsen model 25ST (USA), equipped with a load cell of 5 kN at 1 mm/min crosshead speed. The cellulose nanopaper was cut into a rectangle strip of 10 mm in width and about 40 mm in length. The gauge length between the grips was 20 mm. Five parallel measurements were performed for each film sample at room temperature and ambient conditions. The samples were conditioned for 48 h at 50 % humidity and measured at 20 °C.

Tensile properties of moisture-saturated samples were tested using a Zwick testing machine with a load cell of 2.5 kN at a crosshead speed of 1 mm/min. Tabs from the paper tape were applied to the samples, and the gauge length was set to 20 mm. The elastic modulus was determined in the linear part of the stress-strain curve within the strain range of 0.2–0.5 %. Five replicate samples were tested immediately after their extraction from a desiccator (within 1 min to 2 min) for each NP composition and RH.

A compression test for foam samples was conducted using the Tinius Olsen model 25ST (USA) universal testing machine equipped with a load cell of 5 kN. The cylindrical samples with a height of 25 mm were compressed at a rate of 5 mm/min. Before the testing, the samples were preconditioned for 24 hours at room temperature and ambient conditions. Sandpaper was used to even the sample surface if necessary. The mean result of three specimens for each sample is reported.

Experimental Design and Response Surface Technique

The effect of lignin and xylan on the mechanical properties of the nanopaper was assessed in several stages: (a) the selection of the design parameters and their intervals of variation, (b) the development of the design experiment for the parameters selected, (c) experimental testing, and (d) the determination of the second-order polynomial regression equation.

The full-factorial design (FFD) has been selected, generating nine experimental runs for two parameters and three levels. The minimum and maximum levels for the design parameters are given in Table 2.1.

Table 2.1

Process Parameters and Their Levels

Parameters	**Levels**		
Lignin (wt%)	1	2.5	5
Xylan (wt%)	1	2.5	5

A second-order polynomial regression equation (2.9) has been proposed to predict the response of polymer composites.

$$F(x) = b_0 + \sum_{i=1}^{m} b_i x_i + \sum_{i=1}^{m} \sum_{j=i}^{m} b_{ij} x_i^2 + \sum_{i=1}^{m} \sum_{j=i}^{m} b_{ij} x_i x_j, \qquad (2.9)$$

where $F(x)$ *is* the response, x_i and x_j are the values of parameters, b_0 is the constant, b_i, b_j, and b_{ij} are regression coefficients, respectively, and m is the number of the parameters.

The design parameters and experimental values of specific modulus, specific stress, and strain were determined by averaging the test results of 5 specimens of nanopapers.

3. RESULTS AND DISCUSSION

3.1. Clean manufacturing of cellulose nanopapers by incorporating lignin and xylan as sustainable additives

3.1.1. Tensile properties

The stress-strain curves measured for NP samples are presented in Fig. 3.1. The behaviour of all curves is predominantly linear, consisting of elastic and plastic regions. A substantial increase in the samples' rigidity and material brittleness for lignin, xylan (loadings above 5 wt%), and single and complex filling systems has been observed. It has been suggested that such behavior is caused by decreased slippage yield deformation between the extended cellulose fibrils rather than by covalent bond breakage [42].

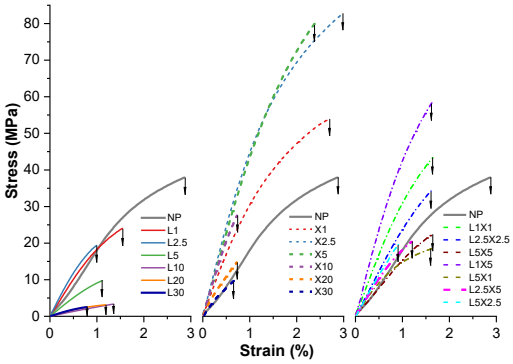

Fig. 3.1. Tensile curves of nanopapers.

In Fig. 3.2, the characteristic tensile properties of elastic modulus, tensile strength, and strain have been summarized to compare single lignin and xylan fillers. Their hybrid materials (LX) are outlined as surface charts in Fig. 3.3.

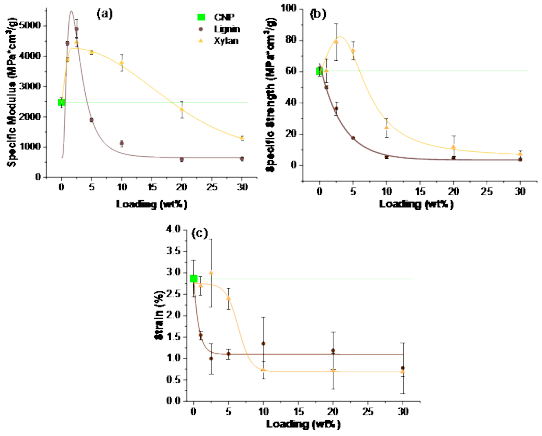

Fig. 3.2. Tensile properties of cellulose nanopapers: specific elastic modulus (a), specific strength (b), and strain (c).

All four xylan compositions with loadings up to 10 wt% showed high specific modulus values, but further addition of xylan resulted in a drop for specific modulus values. Lignin-modified NPs saw decreased specific strength values for all concentrations. Elongation at the break for xylan samples with loading up to 5 wt% remained comparable to CNP, while higher concentrations saw decreased values. All lignin concentrations showed a significant decrease in strain values from 3 % to around 1 % compared to CNP. The decline in elongation values is visible in a shorter plastic region, indicating that some compositions promoted fibril slippage.

Considering hybrid compositions, an in-depth comparison can be made for tensile properties. Using the experimental data as a basis, a response surface plot was constructed for each tensile characteristic to model component contributions. The experimental data obtained in testing were used to construct the second-order polynomial regression equation using the program EdaOpt [43].

Specific elastic modulus, specific tensile strength, and strain graphs (Figure 3.3) show the highest mechanical performance for samples modified with xylan from 2.5 wt% to 5.0 wt% and up to 2.5 wt% added lignin. Surface charts also indicate that up to 1.0 wt% lignin can be added to retain relatively high specific strength and strain values, as other sections discuss the benefits of adding lignin. The strain at break values dropped strongly for hybrid compositions due to the lignin particles' impact on the structure.

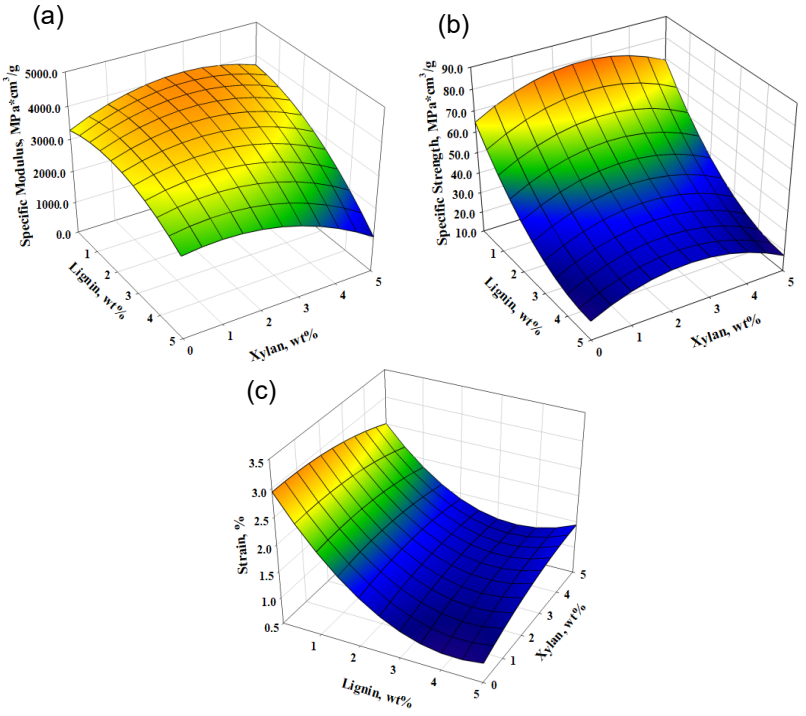

Fig. 3.3. Response surface plots present the results obtained for (a) the specific modulus, (b) specific strength, and (c) strain of the nanopaper with different weight contents of lignin and xylan using the data obtained from regression equations.

3.1.2. Thermooxidative stability

Thermooxidative stability of the nanopaper and its composites was determined using thermogravimetric analysis with a heating rate of 10 °C /min under an oxidative air atmosphere. TGA and derivative weight loss of the prepared nanopaper composites are shown in Figs. 3.4 (a) and (b), respectively.

Lignin is known for its superior thermal stability over other cellulose-based nanoparticles. It is often used for thermal stability enhancement [44,45]. As shown in Fig. 3.4, lignin has the highest thermal stability, but in the case of nanopapers, significant enhancement was not observed before the maximum degradation temperature. Xylan has been identified as the thermally most unstable component of lignocellulose, with the primary degradation step between 200 °C and 370 °C attributed to side-chain unit decomposition, while cracking of the xylan chain backbone is attributed to peak and shoulder with maximum thermal destruction temperature (T_{max}) 250 °C and 296 °C, respectively [46].

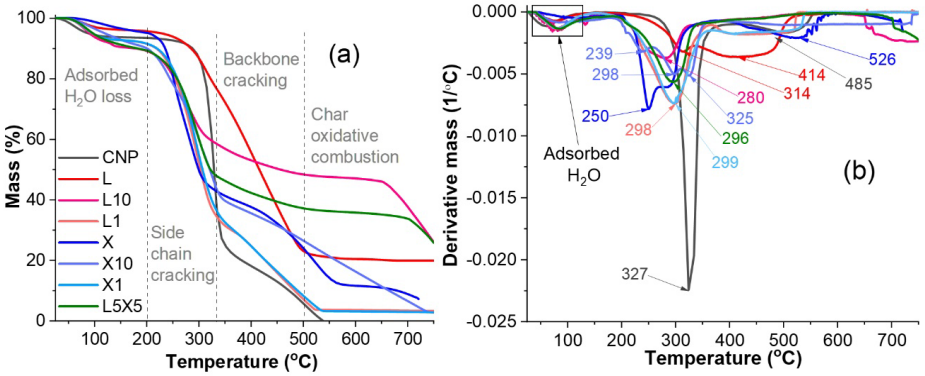

Fig. 3.4. TGA mass (a) and the derivative mass (b) of cellulose (CNP), lignin (L), xylan (X), and hybrid (LX) nanopapers.

3.1.3. Thermal conductivity

Table 3.1 summarizes NPs' density, diffusivity, activation energy (E_a), and inherent conductivity value (λ_0). It has been proposed that the pore size in NPs is too small for air to participate in heat conduction; thus, cellulose crystal orientation and interfacial bonding strength play a significant role in thermal conductivity parameters [47,48]. The film casting process resulted in non-aligned NPs, eliminating anisotropy for thermal properties. The formation of interfaces can be expected from the density of prepared NPs (Table 3.1). The addition of 1 wt% lignin decreased density to 0.48 g/cm^3, the lowest value observed from prepared NPs.

While loading more lignin increased density value, they remained comparable to CNP. Lignin resulted in various defects like voids, which contributed to higher porosity and lower density values. Xylan is a shorter, more branched molecule that can fill gaps between NFC networks and increase interfacial bonding; this is reflected as a loss of porous structure and significantly increased density in the range from 0.89 g/cm^3 to 1.36 g/cm^3 showing a 1.4 to 2.2-fold increase compared to CNP. The changes in thermal conductivity coincide with density changes (Fig. 3.5), as NPs with higher density show higher values.

Table 3.1

Density, Diffusivity (at 25 °C), Specific Heat (at 25 °C), Activation Energy E_a and Inherent Conductivity Value λ_0 of Cellulose Nanopapers

Sample	Bulk density (g/cm^3)	Diffusivity (mm^2/s)	λ_0 (W/(m·K))	E_a (kJ/mol)
CNP	0.63 ± 0.06	0.091	0.27	3.59
L1	0.48 ± 0.03	0.096	0.22	3.61
L2.5	0.52 ± 0.03	-	-	-
L5	0.55 ± 0.03	-	-	-
L10	0.61 ± 0.05	0.167	0.42	4.01
L20	0.63 ± 0.04	-	-	-
L30	0.66 ± 0.07	0.142	0.22	1.89
X1	0.89 ± 0.06	0.099	0.51	2.64
X2.5	1.05 ± 0.04	-	-	-
X5	1.09 ± 0.03	-	-	-
X10	1.14 ± 0.04	0.180	2.73	6.81
X20	1.24 ± 0.04	-	-	-
X30	1.36 ± 0.03	0.161	1.16	3.93
L1X1	0.64 ± 0.04	0.076	0.50	5.54
L1X5	1.01 ± 0.04	-	-	-
L5X1	0.6 ± 0.03	-	-	-
L2.5X25	0.69 ± 0.05	-	-	-
L2.5X5	0.99 ± 0.02	-	-	-
L5X2.5	0.79 ± 0.04	-	-	-
L5X5	0.89 ± 0.03	0.103	0.49	4.90

Figure 3.6 was used to determine E_a values utilizing the slope of the approximate straight lines in the Arrhenius plot. While λ_0 was calculated from the Arrhenius equation using the method described in [49]. The activation energy indicates the role of distributed nanoparticles in NPs for composite insulation properties as another layer blocks or promotes heat transfer [50]. Thus, λ_0 and E_a values depend on the nanoparticle's nature or formed agglomerates or layers in case of high loadings. Table 3.1 indicates a 1.9-fold decrease of activation energy was achieved for the L30 sample, while X10 saw a 1.9-fold increase. E_a did not show a strong correlation with thermal conductivity, but this can be explained by significantly altered microstructure. Most of the sample's activation energy increased similarly to thermal conductivity and diffusivity. Lignin compositions showed either negative trends or similar results to CNPs.

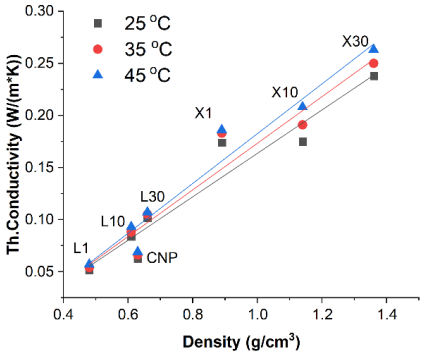

Fig. 3.5. Thermal conductivity vs. bulk density of cellulose (CNP), lignin (L), and xylan (X) nanopapers.

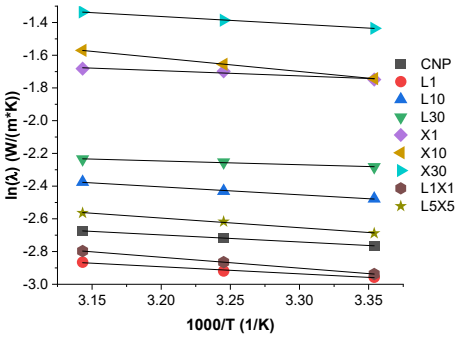

Fig. 3.6. Arrhenius plot: dependence of thermal conductivity on temperature for cellulose (CNP), lignin (L), xylan (X), and hybrid (LX) nanopapers.

3.1.4. Summary

Wastepaper has huge potential to be an excellent source for nanopaper production and fits the circular economy goals. It should be noted that in addition to cellulose, wastepaper can also contain several impurities, such as inorganic fillers, glues, pigments, and laminated polymers, which greatly complicates recycling and the technological process of extracting pure cellulose. Water suspensions have a significant advantage over other studies implementing various organic solvents. Using lignin and xylan solutions for nanopapers shows multiple benefits as they act more as surface modification agents. Their high loadings are disadvantageous due to phase separation and the heterogeneous structure of these nanopapers. Lignin introduces defects and heterogeneous elements, while xylan fills gaps between cellulose fibrils to create a more homogenous system. The structural changes induced by adding xylan reduce light scattering and yield transparent nanopaper. Defects caused by lignin remain in the structure, while xylan seems to lower the size of formed voids and isolate them. The use of lignin can increase stiffness, resulting in decreased tensile strength and elongation values. The densification of the structure leads to an increase in thermal conductivity. The obtained nanopaper with tunable morphology has shown great perspectives as packaging materials and filters. They would also benefit from developing clean manufacturing routes from waste sources.

3.2. Lignin and xylan as interface engineering additives for improved environmental durability of sustainable cellulose nanopapers

3.2.1. UV irradiation and heat effect on the tensile properties

Figure 3.7 depicts sample stress-strain curves, and Fig. 3.8 illustrates tensile properties for UV-irradiated samples. For the reference samples, the effects of lignin and xylan modifiers can be examined for their tensile properties, which indicate that the addition of xylan enhances all tensile properties. In contrast, lignin reduces the elastic modulus and tensile strength but increases the elongation at break values (Fig. 3.8). The addition of xylan to CNP showed an increase in NP's properties even with high loading up to 20 wt% for the specific elastic modulus and specific tensile strength, achieving up to 1.4-fold and 2.8-fold improvements, respectively. Elongation values reach a maximum value at 10 wt% xylan loading, showing a 2.8-fold improvement compared to CNP. In comparison, lignin addition resulted in a 2.6-fold increase in the elongation values, while specific elastic modulus exhibited a 1.1 to 3.6-fold decrease for lignin content up to 10 wt%. Specific tensile strength showed similar values to CNP with loadings up to 5 wt% lignin, but further addition resulted in almost a 2-fold decrease. At higher lignin loadings, samples were fragile and showed a further drop in properties. It was observed that modifier loading of 10 wt% corresponds to the xylan critical threshold concentrations for the developed interface structure.

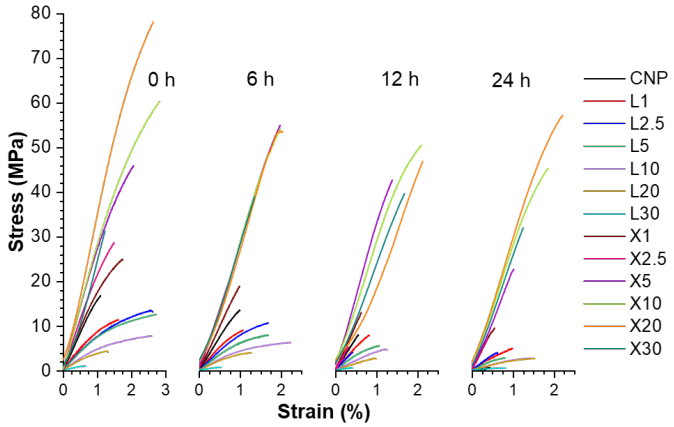

Fig. 3.7. Representative stress-strain curves of NP for pristine and aged samples at different times of UV irradiation at 80 °C temperature.

UV-irradiated CNP showed a catastrophic decrease in properties, and after 24 hours of UV exposure, its properties were the lowest of any NP. The literature has reported that cellulose is very unstable in UV light without stabilization additives [51-53]. The aged xylan NP samples demonstrated a shift to lower filler loadings that achieved the best properties. For xylan NPs, the best values after aging were for loadings from 5 wt% to 20 wt%. Lignin-modified NPs showed a slight increase in elongation values and decreased elastic modulus and tensile strength compared to CNP. In addition, it was also observed that xylan loadings up to 5 wt% benefited from exposure to UV, resulting in the stiffening of NP.

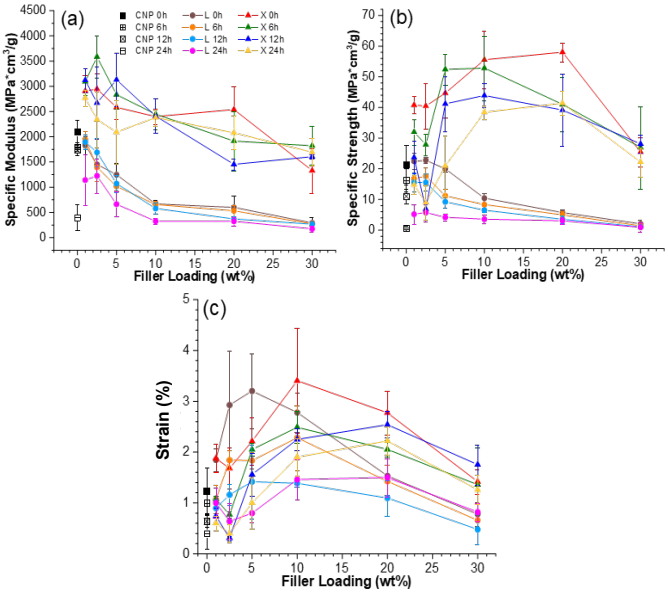

Fig. 3.8. Tensile properties: (a) specific elastic modulus, (b) specific ultimate tensile strength and (c) elongation at break for nanopapers before and after exposure to intensive UV irradiation at 80 °C.

3.2.2. Structural analysis

Figure 3.9 shows a typical scanning electron micrograph of selected NP compositions. SEM images revealed closely packed cellulose fibrils with an interconnected network that showed visible porosity and no structural deformations. The introduction of lignin in L5 NP shows that a small layer of lignin nanoparticles has been accumulated on the surface of cellulose fibrils and in the previously visible pores. The addition of lignin has contributed to visible layer delamination and the formation of microscale voids. This explains the decreased mechanical performance observed for lignin NP. The L30 NP SEM images reveal a strongly disrupted cellulose fibril network with a chaotic structure that includes large voids.

In contrast, the addition of xylan to CNP showed a densely packed structure with no visible pores or voids in the structure of X10. Our observations coincide with the literature, where xylan shows the ability to fill gaps between cellulose fibers and improve properties in low loadings [54,55]. The smaller molecular weight and more branched structure contribute to xylan's ability to insert itself into gaps between cellulose fibers and coat them. In addition, xylan effectively enhances the hydrogen bond network of cellulose, thus, there is no visible separation between xylan and cellulose in X10 NP. At the same time, X30 NP shows clear phase separation, and xylan forms visible interphase layers. Xylan's ability to form dense structures with no visible pores could be used to improve gas barrier properties by adding or coating [56].

The surface morphologies of unaged and aged NP have been studied by SEM (Fig. 3.10). The 24-hour irradiation and heat treatment were chosen to maximize differences between the

compositions. The unaged NP surface yields similar observations to those previously discussed above. Before aging, all NPs showed a relatively smooth surface with interconnected cellulose fibers. After aging, the CNP surface becomes very rough, and individual fibers become more pronounced, which indicates that small fibrils connecting large fiber formations have degraded. The observed catastrophic failure of mechanical performance properties reflects the loss of interconnected fibre networks.

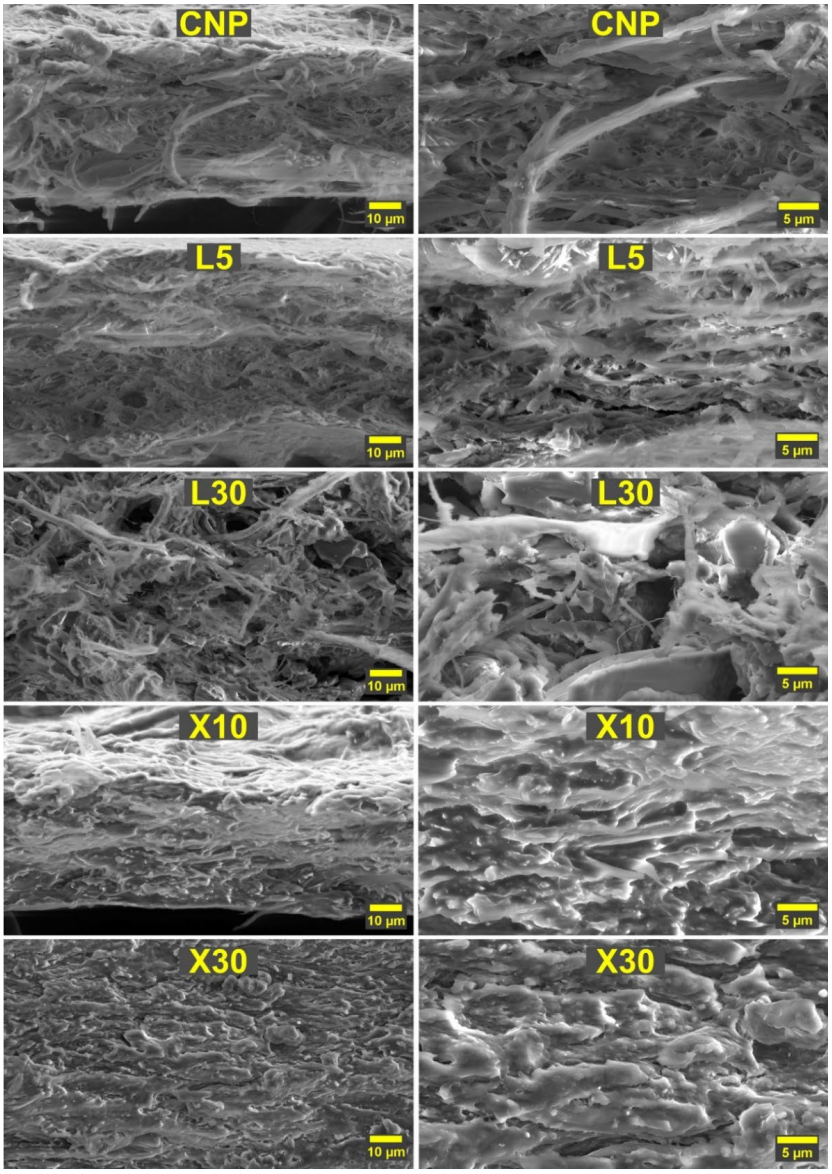

Fig. 3.9. Cross-section scanning electron micrographs of selected NP compositions.

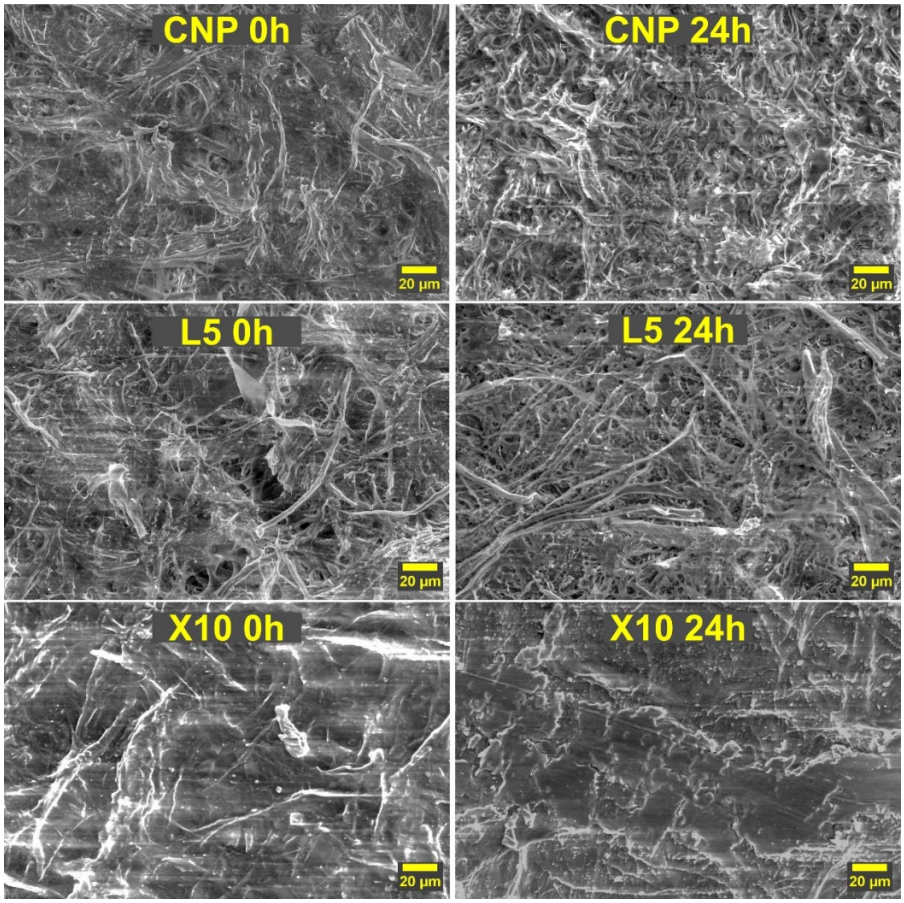

Fig. 3.10. The impact of 24 hours of UV irradiation on the surface morphologies of selected NP compositions.

3.2.3. FTIR spectroscopy

Figure 3.11 shows the FTIR spectra of NP samples before and after 24 h of UV irradiation, while Table 3.2 summarizes the absorption band assignments. L5 and X10 samples were selected for the FTIR analysis due to their mechanical property preservation compared to CNP. The spectra for CNP show the highest absorption at 1000 cm^{-1} to 1100 cm^{-1} region, indicating characteristic cellulose peaks for C-O linkages. The addition of lignin reduces the intensity of these peaks, indicating partial surface coating. At the same time, lignin aromatic ring C=C double bond stretching (7) is introduced in the L5 spectra [57]. In contrast, adding xylan alters the characteristic double C-O peak intensities and introduces a new C-O peak at 976 cm^{-1}, which is commonly used for xylan identification [58]. Both modifiers influenced the -OH group absorption, further proving changes in surface structure and hydrogen bond formation.

Table 3.2

Assignments of the Infrared Absorption Bands

Band	Wavenumber (cm^{-1})	Assignment	Reference
1	3333	Intramolecular hydrogen bonding of -OH group	[59]
2	3276	Intermolecular hydrogen bonding -OH group	[59]
3; 4	2915, 2850	CH symmetrical and asymmetrical stretching	[59]
5	1738	C=O stretching of acetyl or carboxylic acid in hemicellulose	[60]
6	1640	C=O stretching in the carboxyl group	[61]
7	1582–1560	C=C stretching of lignin aromatic ring	[57]
8	1458	CH bending of Xylan	[58]
9	1427	CH_2 scissoring	[59]
10	1372	C-H bending	[59]
11, 22	1315, ~ 700	CH_2 rocking	[53,59]
12, 13, 15, 16, 17	1242, 1202, 1110, 1055, 1030	C-O stretching	[58,59,61]
14	1160	C-O-C asymmetric bridge	[60]
18	976	C-O stretching in Xylan	[58]
19	895	β-Linkage of cellulose	[59]
20, 21	837, 776	C-H out of plane deformation in lignin aromatic ring	[58,62]

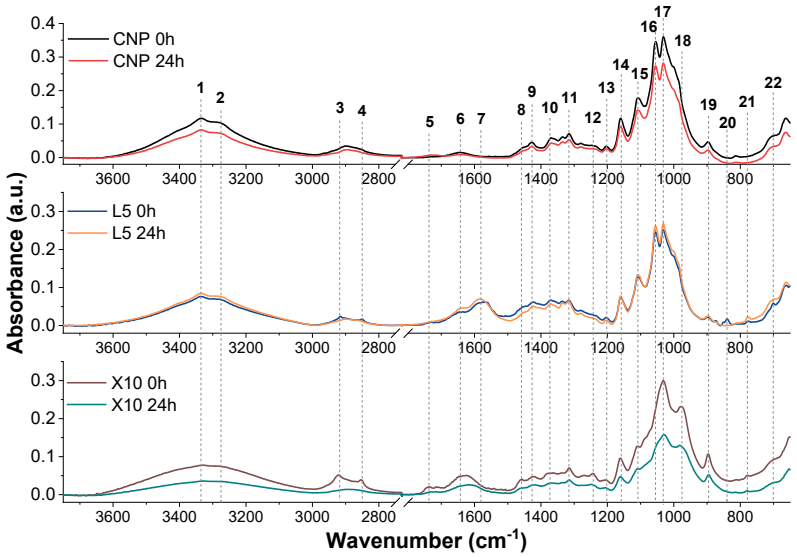

Fig. 3.11. FTIR spectra of CNP, L5 and X10 samples before and after 24 h UV irradiation.

3.2.4. Moisture effect on the tensile properties

Tensile tests were conducted after stabilising the sample weight under three selected RH values: 24 %, 75 %, and 97 %. A comparison of tensile properties in different RHs for NPs is presented in Fig. 3.12. Moisture absorption greatly affected the mechanical behavior of the NPs, resulting in a decrease in the elastic and strength characteristics with higher water saturation. Lignin-modified NPs are characterized by lower tensile properties and a higher sensitivity to moisture than the CNP. This results in a complete loss of operation properties of highly loaded lignin NPs, making these compositions almost unusable at high RH. The addition of xylan, on the contrary, improved the mechanical characteristics of CNP.

Specific elastic modulus values increase by 32 % and 55 % for X2.5 NP compared to CNP at RH 24 % and RH 75 %, respectively. Absorbed moisture plasticized the material, although the elastic modulus and strength of moisture-saturated (RH97 %) xylan NPs are comparable to CNP. For lignin NPs, a decrease in the elastic modulus and tensile strength was observed. Correspondingly, Xylan NPs showed a remarkable 2.3-fold increase in specific tensile strength at RH75% for X2.5 composition. Tensile strength was comparable to CNP at RH 97 %, similar to changes observed for elastic modulus. Elongation values showed an opposing trend and increased with moisture content. Lignin NPs still had lower values than CNP, but xylan NPs showed comparable values. All strain measurements showed relatively large data scatter, as indicated by error bars.

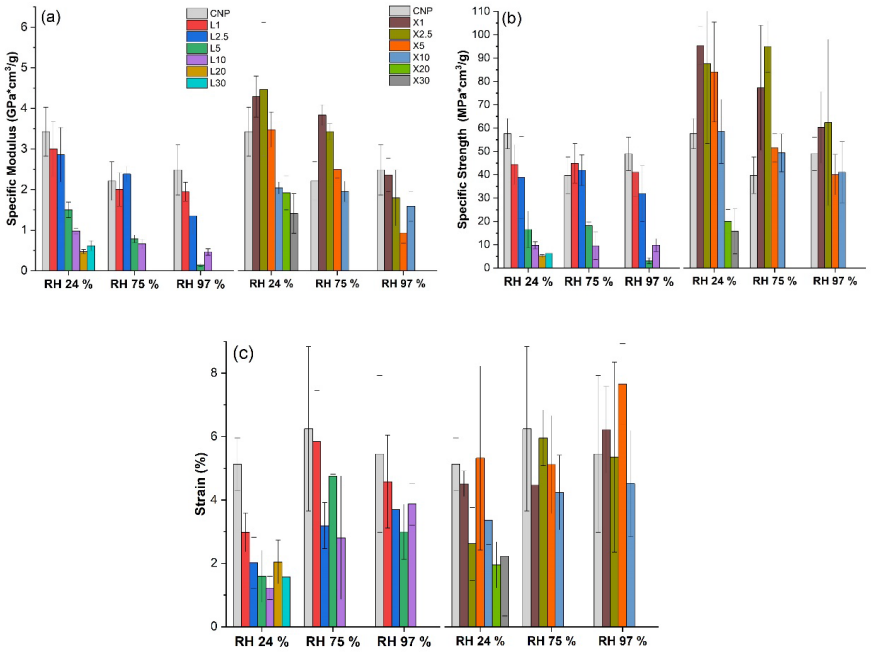

Fig. 3.12. Tensile properties: (a) specific elastic modulus, (b) specific ultimate tensile strength, and (c) elongation at break for NPs saturated under different RH.

3.2.5. Summary

The proposed cellulose nanopaper modification, using lignin and xylan additives, provides a simple and sustainable route to engineer the interface in the developed mesh material and control the material's durability to the UV irradiation, moisture, and temperature. The tensile properties are significantly enhanced with the addition of xylan and lignin interface modifiers. The UV irradiation showed a milder impact on the cellulose modifications with 5 wt% and 10 wt% xylan concentrations. The moisture absorption test showed the overall best performance for xylan's 2.5 wt% compositions. Xylan interface development in all sample concentrations showed remarkable improvements in NP UV and heat resistance. Lignin also enormously improved the UV resistance of NP. Cellulose NP without interface modifiers exhibited a catastrophic decrease in tensile properties after UV exposure. The UV irradiation damage is revealed in SEM analysis.

The oxidation and depolymerization of lignin and xylan at the protective interface for the cellulose was indicated by FTIR spectroscopy as a shift in absorption peak intensities and regions. The moisture sorption capacity of the NP increases with moisture level and with lignin and xylan loadings. High moisture content promoted NP swelling, which failed samples with 20 wt% and 30 wt% loadings of lignin and xylan. Absorbed moisture significantly affects the elastic modulus and strength characteristics of CNP, but resistance was improved for modified NP. The lignin modifier resulted in higher moisture absorption capacity and, as a result, higher properties' sensitivity to humidity changes due to the strong agglomeration and phase segregation effect. But remarkably, lignin NP showed better property retention even at high moisture content compared to CNP. Retention of the elastic modulus and strength after moisture desorption is in the range of 60–95 %; lignin-modified compositions show the highest property retention.

The NP films of X10 and L2.5 have presented the highest durability performance characteristics against UV irradiation and humidity aging. The improvements were achieved by improving the interface (xylan) while the developed interphase layer covered the cellulose mesh.

3.3. Sustainable hemp-based bioplastics with tunable properties via reversible thermal crosslinking of cellulose

3.3.1. Thermal stability and crosslinking characterization

As chemical crosslinking was performed at relatively high temperatures, selected compositions were tested for thermal stability in the air. Thermogravimetric weight loss and derivative weight loss curves are presented in Fig. 3.13. The initial weight loss that occurs between 80 °C and 120 °C is attributed to the evaporation of the remaining water [63]. Around 220 °C, the initial decomposition of the main components starts. This initial step is attributed to the degradation of hemp and xylan components, especially hemp, which consists of various carbohydrates and lignin [64].

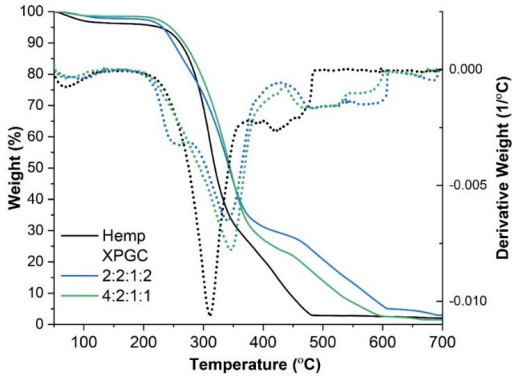

Fig. 3.13. Thermogravimetric curves of hemp paper and selected bioplastics.

The impregnated components and formation of a crosslinked network contribute to the shifting of the main degradation peak by around 40 °C. The crosslinking process increases the molecular weight of carbohydrates, thus increasing the time needed for the polymer network degradation. For composition 2:2:1:2, the initial degradation step occurs before hemp and 4:2:1:1. The presence of low molecular weight components can explain the difference between the initial degradation step for compositions. The difference is only 20 °C, indicating that the impregnated composition 4:2:1:1 is slightly more stable due to different ratios. At the same time, both bioplastics show main degradation peak T_{max} (temperature with maximum weight loss) at around 350 °C.

The formation of the polymer network can be evaluated from dynamic rheological parameters, such as G' (storage modulus), G'' (loss modulus), and η* (complex viscosity). The rheological properties were determined during isothermal curing with a fixed temperature of 140 °C (same as sample curing temperature) as a time sweep measurement. Graphs of log G', log G'', and tan δ versus time were recorded for selected compositions (impregnated mixtures). Figure 3.14 shows G', G'', and tan δ curves for 2:1:2:2 and 4:4:1:2.

At the start, the moduli decrease slowly, which might seem a bit strange behavior but can be explained by water evaporation, thus delaying the start of the reaction. For 2:1:2:2, the water evaporation lasted about 20 min, while for other compositions, it occurred for 1 to 2 hours. The

confined nature of the parallel plates of the rheometer significantly influences evaporation time. In Fig. 3.14 (b), tan δ does not show any systematic variation until 1 h, further indicating that the reaction does not occur till that point. After water evaporates, G' and G'' curves are relatively close to each other, thus indicating a region where the formation of a 3D network occurs. The third region in the graphs represents the separation of G' and G'' curves, where G' values significantly exceed G''. As the reaction approaches the complete state, the elastic properties dominate, more energy is stored, and less energy is dissipated ($G' > G''$).

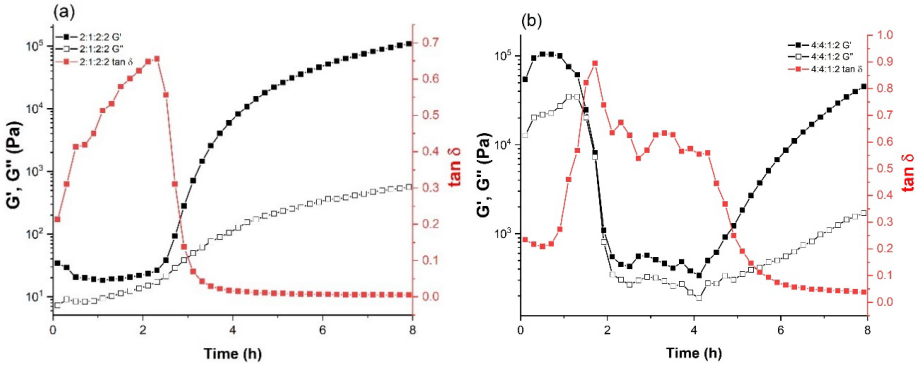

Fig. 3.14. Rheological parameters G', G'', and tan δ for (a) 2:1:2:2 and (b) 4:4:1:2 impregnated mixtures.

The molecular characterization of the initial reactive composition and the final crosslinked network was characterized by FTIR analysis. Figure 3.15 shows the FTIR spectra of hemp, not crosslinked 2:1:2:2, and selected bioplastics. Figure 3.15 (a) shows spectra overlays indicating several key shifts, which indicate that the crosslinking reaction was successful. The decrease in intensity for hydroxyl group (OH) stretching vibrations with a broad peak at around 3330 cm^{-1} and a shifted peak at 1732 cm^{-1} representing the formation of ester's carbonyl group (C=O) can be considered signature peaks for the crosslinking reaction [65]. Thus, it confirms a successful crosslinking reaction for prepared bioplastics.

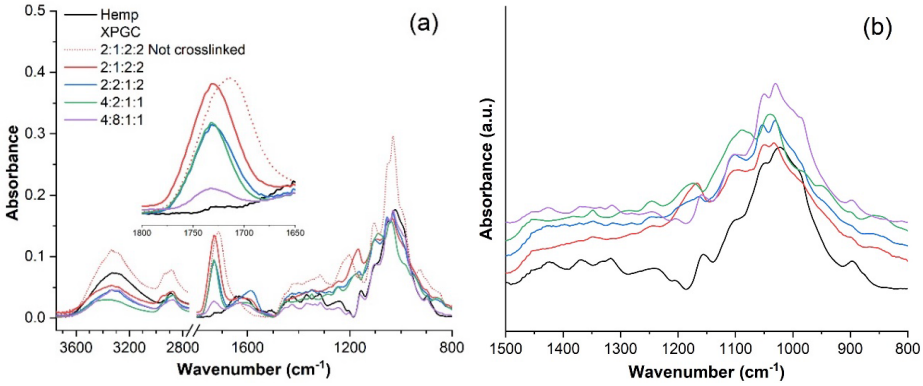

Fig. 3.15. FTIR spectra of hemp paper and bioplastics: (a) spectra overlay showing a full range of scans and (b) stacked spectra showing the region from 1500 cm^{-1} to 800 cm^{-1}.

3.3.2. Structure and morphology

Four distinct bioplastics and hemp paper were selected for SEM analysis based on tensile properties. Figure 3.16 shows cross-cut micrographs of selected samples with 500× and 2500× magnifications. Hemp paper's structure shows a relatively dense fiber structure with visible porosity. The porosity for all samples and their respective density values are shown in Table 3.3.

SEM micrographs show that the nanofibrillated structure has been rearranged into larger fibres with a diameter of around 1 μm, while the length is in the tens to hundreds of micrometres. Bioplastics undergo several processes, including impregnation, thermal crosslinking, washing in water, swelling, and drying. The dimensional changes of samples showing an increase in thickness are attributed to sample swelling. The structure has large pores and visible swelling, which can be seen as the separation of hemp fibres. The other three selected compositions show relatively dense structures with coated hemp fibres that are hard to distinguish in images. Even 4:2:1:1 with a lower amount of citric acid shows a relatively dense structure, thus further indicating that PEG is the main component that limits cross-linking. The structure of 4:2:1:1 retains visible porosity, and it is also the only bioplastic with a separate layer of impregnated composition deposited on the surface. The structures of 2:1:2:2 and 2:2:1:2 are relatively similar, showing uniform impregnation and dense structure, which was retained after 48 h in water. The observed structures align with the FTIR results, showing denser packing with a higher crosslinking degree.

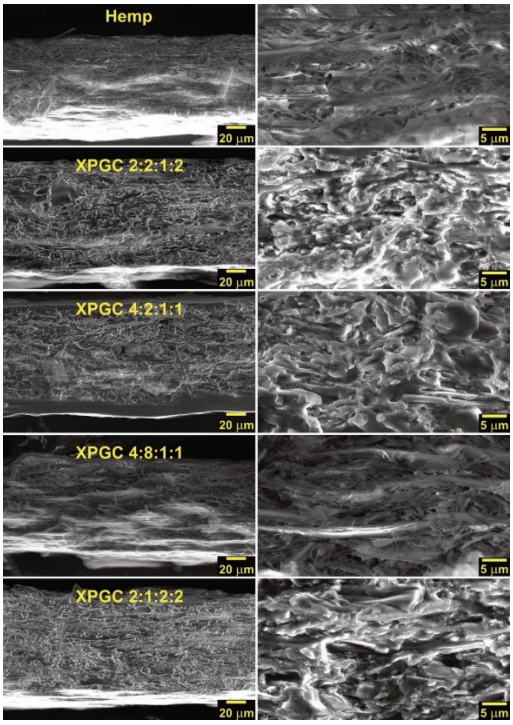

Fig. 3.16. SEM micrographs of hemp paper and selected bioplastics shown in 500× and 2500× magnifications.

3.3.3. Tensile properties and water uptake

Water absorption and swelling in water are often considered the biggest issue for various cellulose-based materials. Table 3.3 shows measured elastic modulus, tensile strength, and elongation values. Figure 3.17 (a) shows tensile stress-strain curves for selected three compositions before and after being submerged in water. "Neat" denotes compositions as they were before washing in water. After being submerged in water and dried, all three tested compositions showed a significant increase in elastic modulus and tensile strength, while strain values were relatively unchanged.

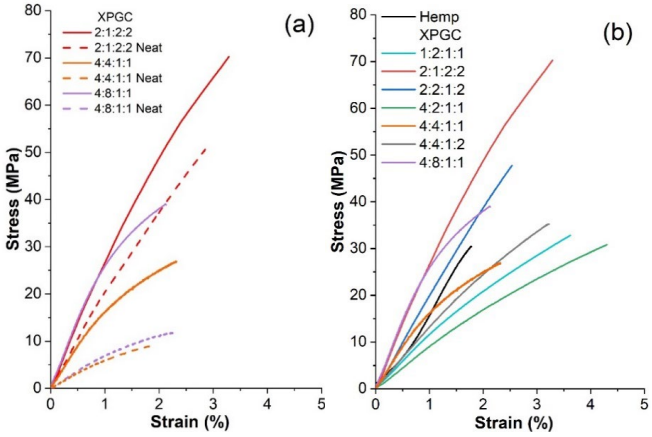

Fig. 3.17. Tensile stress-strain curves for (a) selected bioplastics before and after washing in water and (b) hemp paper and bioplastics.

Figure 3.17 (b) compares stress-strain curves for all seven impregnated compositions and hemp paper, and Table 3.3 shows their respective elastic modulus values. The data indicate that bioplastic properties can be significantly tuned compared to hemp paper, achieving up to 2.3-fold improvement in tensile strength value, up to 1.8-fold for elastic modulus, and up to 2.4-fold for elongation. In addition, six compositions showed enhanced tensile strength values, and all seven had enhanced elongation values.

Water uptake was further tested for material durability. Thin bioplastic samples achieved equilibrium water uptake after 24 h and retained similar values for 30 days. Water uptake percentage and sol content are shown in Table 3.3. All bioplastics have significantly reduced water uptake compared to hemp paper. This is because hemp paper slowly swells in water, while bioplastics retain their shape due to chemical crosslinking. Most notable is composition 2:1:2:2, which achieved a 7-fold decrease in water uptake. Sol content represents a mass of composition that was washed out from the composition after thermal curing. These values correlate well with water uptake and SEM microstructure, where 2:1:2:2 and 4:8:1:1 represent both ends of property dispersion. Some impregnated compositions stick better to the surface and form denser structures; this could explain variations in sol values.

Table 3.3

Apparent Density, Porosity, Sol Content, Water Uptake, and Tensile Test Parameters for Hemp Paper and Bioplastics

Sample	Apparent density (g/cm^3)	Porosity (%)	Sol content (wt%)	Water uptake (%)	Elastic modulus (MPa)	Ultimate tensile strength (Mpa)	Strain at break (%)
Hemp	0.73 ± 0.04	51.3	-	143.0 ± 3.2	1660 ± 190	30 ± 3	1.8 ± 0.2
XPGC							
1:2:1:1	1.08 ± 0.02	25.4	15.4 ± 3.2	63.2 ± 2.1	1176 ± 128	33 ± 4	3.6 ± 0.3
2:1:2:2	1.07 ± 0.07	27.5	6.7 ± 2.1	20.4 ± 1.3	2828 ± 348	70 ± 7	3.3 ± 0.6
2:2:1:2	1.21 ± 0.05	17.3	10.2 ± 1.6	73.1 ± 9.4	2040 ± 339	48 ± 6	2.5 ± 0.4
4:2:1:1	1.34 ± 0.17	-*	18.8 ± 2.5	63.1 ± 1.6	913 ± 156	31 ± 3	4.3 ± 0.1
4:4:1:1	0.82 ± 0.04	44.7	24.3 ± 2.8	78.8 ± 1.8	1840 ± 236	27 ± 2	2.3 ± 0.4
4:4:1:2	1.19 ± 0.02	18.0	22.4 ± 2.2	56.9 ± 3.4	1350 ± 120	35 ± 2	3.2 ± 0.3
4:8:1:1	0.78 ± 0.03	47.5	54.7 ± 4.1	100.2 ± 7.6	2927 ± 271	39 ± 2	2.1 ± 0.2

* Precise calculation was not possible due to the unique morphology of the sample.

3.3.4. Depolymerization and recycling

The depolymerization route was examined as an alternative to the biodegradation route to promote sustainable material management and incorporate a circular approach to generated waste. Bioplastics were inserted in alkaline and acidic solutions and neutral water. While testing water uptake and leaching, we observed that bioplastics stay stable at 20 °C for at least one month in water environments. Alkaline ester hydrolysis was tested with NaOH (0.5 mol/L) solution at 20 °C, and it was observed that surface-impregnated compositions degrade rapidly between 10 min to 1 hour, yielding hemp-cellulose pulp. The sample loses color and shifts to an off-white color, and fibers separate over time, resulting in a pulp-like mass formation. The pulp can then be filtered, recovered, and used for new material preparation. Acidic ester hydrolysis was tested with HCl (0.5 mol/L) solution, but even heating at 80 °C for 6 h did not depolymerize the bioplastic's structure. Treatment with an HCl solution slightly changed the surface color of the sample. The images of depolymerized samples and the proposed recycling route are shown in Fig. 3.18.

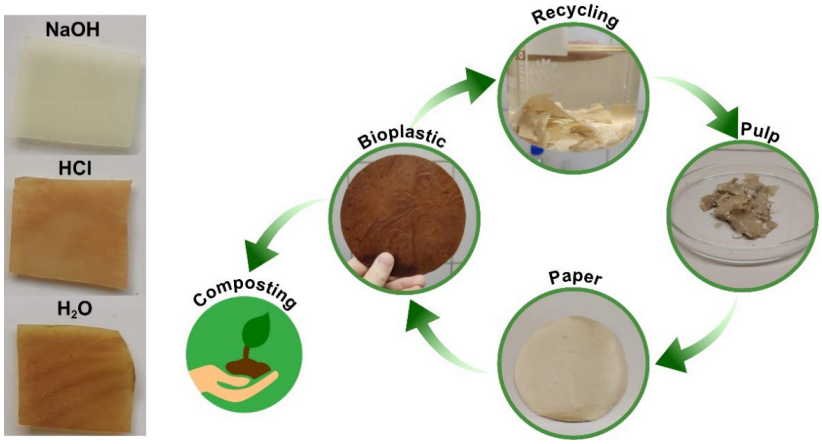

Fig. 3.18. Proposed recycling route and pictures showing alkaline and acidic solution impact on bioplastics.

3.3.5. Summary

This study investigates the performance of hemp bioplastics, consisting of hemp paper impregnated with seven varied ratio compositions of xylan, PEG, glycerol, and citric acid. Based on the experimental results, the following conclusions are presented:

I. FTIR indicates the formation of ester bonds and successful crosslinking reaction; at the same time, reduction in hydroxyl group signal intensity complements this observation. Rheology studies at 140 °C show that the initial crosslinking reaction starts after water evaporation and that around 2 to 3 h are needed after water evaporation to reach gelation, while for complete crosslinking, more than 6 h are needed.

II. The bioplastics show exceptional resistance to water, preserving their dimensional stability. While submerged in water, bioplastics lost 7 wt% to 55 wt% (sol content). Surprisingly, after washing samples in water for 48 h, tensile strength and elastic modulus significantly increased while retaining about the same enhanced elongation values. The highest achieved tensile values show an elastic modulus of 2.9 GPa, a tensile strength of 70 MPa, and an elongation of 4.3 %. Tensile failure indicates a high degree of tunable properties as materials range from brittle to ductile.

III. Impregnation results in a very dense structure resistant to water uptake, showing up to a 7-fold reduction. The excess amount of PEG results in the porous structure of hemp paper being preserved while gaining crosslinked stability. This opens a research direction that could be exploited to prepare membranes and filters.

3.4. From wood and hemp biomass wastes to sustainable nanocellulose foams

3.4.1. Structural characterization

Figure 3.19 (a)–(b) shows the optical microscopy micrographs of the prepared microcellulose powders, while Fig. 3.19 (c)–(d) shows STEM micrographs of nanolignocellulose fibrils obtained from wood and hemp microcellulose powders. The measured length of hemp fibers is 372 μm, which is twice as long as raw wood fibers, which is 181 μm (Table 3.4). Wood particles are shorter in length (L) and narrower in fiber diameter (D). Thereto, their calculated L/D ratio is smaller. The NFC parameters are summarized in Table 3.5, evidence that the nanofibrils' average diameter is 123 nm and 70 nm for wood NFC and hemp NFC, correspondingly. The coagulation stability of the prepared dispersions of the hemp and wood NC fibrils in water was evaluated employing the zeta potential (ζ) [66,67]. The obtained ζ are also represented in Table 3.5. Reported data are average values of all measured NFC suspension concentrations. The zeta potentials received for wood and hemp NFC samples are –23.6 mV and –22.6 mV, respectively.

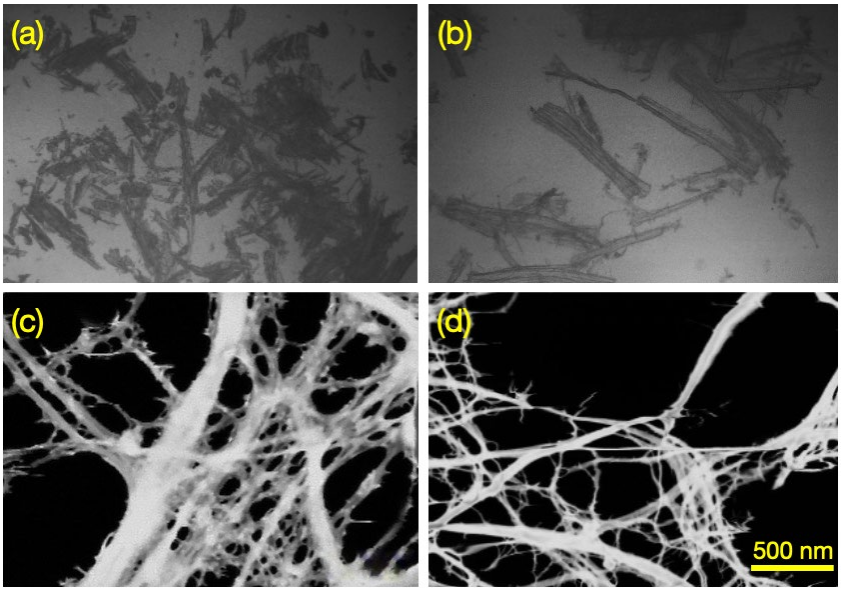

Fig. 3.19. Optical microscopy micrographs (a, b) of microcellulose powders and TEM (c, d) micrographs of NC obtained from wood (c) and hemp (d) waste.

Table 3.4

Geometrical Dimensions and Aspect Ratio of Wood and Hemp Waste Powders

Sample	Length (μm)	Diameter (μm)	Aspect ratio (L/D)
Wood	181 ± 86	30 ± 16	7 ± 5
Hemp	372 ± 183	48 ± 23	9 ± 5

Table 3.5

STEM Measured Fibril Diameter and Zeta Potential of Obtained Wood and Hemp NFCs' Water Suspensions

Sample	Diameter (nm)	Zeta potential (mV)
Wood NFC	123 ± 50	–23.6 ± 8.6
Hemp NFC	70 ± 32	–22.6 ± 8.2

3.4.2. X-ray diffraction (XRD) analyses

Figure 3.20 shows the XRD pattern and the calculated corresponding crystallinity indices (CI) of raw samples (without alkaline treatment) and for wood and hemp fibrils. All NFC samples show typical cellulose I structure with the characteristic diffraction peaks of 2θ angles at around 16° and 22° corresponding to the (101) and (002) planes. According to literature, it is expected to see three peaks at about 15°, 16° and 22° corresponding to (101), ($10\bar{1}$), and (002) planes, respectively [41], but as it can be observed, the presence of non-cellulosic substances such as hemicellulose and lignin causes the merging of two distinct diffraction peaks at 15° and 16° into a single diffraction peak at 16° [68]. Besides, the hemp NFC sample with very low hemicellulose and lignin content has two distinct diffraction peaks at 15° and 16°.

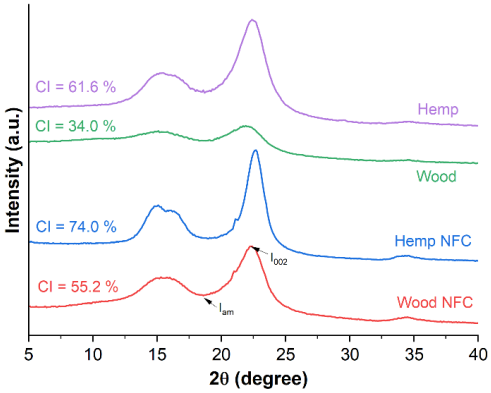

Fig. 3.20. XRD curves of raw wood and hemp and wood NFC and hemp NFC: purple – raw hemp; green – raw wood; blue – hemp NFC; red – wood NFC.

3.4.3. Thermal analysis

The TGA and DTG curves obtained from the thermogravimetric analysis of the wood and hemp samples are shown in Fig. 3.21 (a) and (b), respectively. All the samples show two pronounced characteristic steps of weight loss. The first one is detected in the range of 40–130 °C with 5–6 % weight loss, which corresponds mainly due to the evaporation of adsorbed water in the NC [69]. The calculated onset and main degradation temperature data are represented in Table 3.6.

The process of the degradation of the samples starts at a range of 250–260 °C, which shows as a small shoulder in DTG curves for wood samples, indicating degradation of hemicellulose [46]. A significant weight loss is observed in the second step, with the main degradation

temperature at around 333 °C, which corresponds mainly to NC degradation [69]. All NC samples show roughly the same degradation onset degradation temperature at about 255–260 °C, and the TGA weight loss curve difference is not significant at the degradation temperature either, except for hemp NFC. NFC hemp shows a higher degradation onset temperature at around 274 °C, and the weight loss after 350 °C is significantly higher than other NC samples, which is also seen in the DTG graph (Fig. 3.21 (b)).

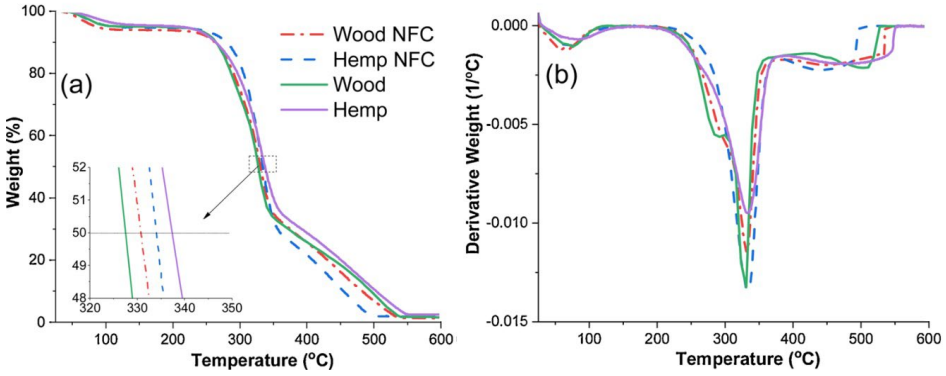

Fig. 3.21. Thermogravimetric weight loss (a) and differential thermogravimetric (b) curves.

Table 3.6

Thermal Degradation Characteristics of Wood and Hemp Waste Powders and Wood and Hemp NFC

Sample	The onset of degradation temp. (°C)	Main degradation temp. (°C)	Residue at 450 °C (%)	Residue at 600 °C (%)
Wood	254	328	18.10	1.63
Wood NFC	259	332	16.18	1.39
Hemp	253	333	20.19	2.42
Hemp NFC	274	333	10.98	1.82

3.4.4. Foam material morphology characterization

The physical characteristics of the obtained wood and hemp NC foams are provided in Table 3.7. The bulk density was in the range of 2–11 mg/cc for hemp NFC foams, while values were higher at 4–36 mg/cc for wood NFC samples produced from comparable concentrations. The porosity for all samples was above 99 %. SEM micrographs of wood and hemp foams with their respective bulk densities in the range of 2–36 mg/cc are shown in Fig. 3.22. The obtained wood and hemp foams have an obvious mesh-like network porous structure made of entangled cellulosic nanofibrils.

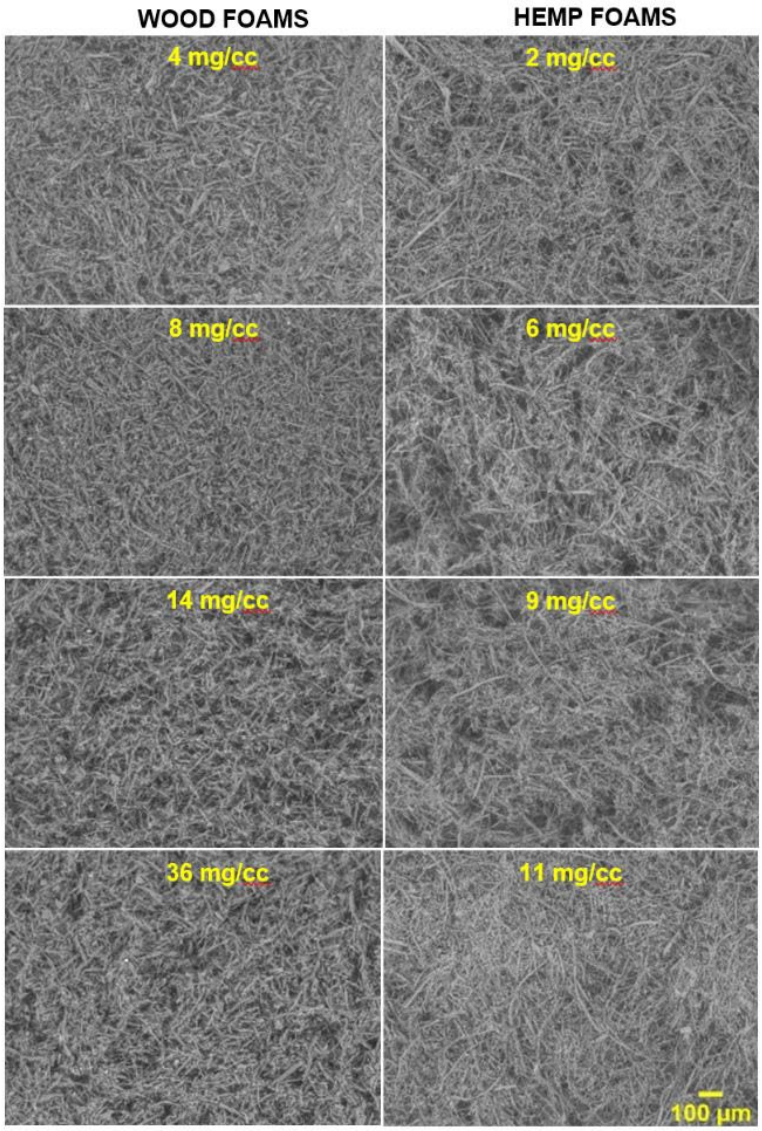

Fig. 3.22. SEM micrographs of wood and hemp foams at 100x magnification.

3.4.5. Compression properties

The mechanical behavior of obtained highly porous NC foams was studied by compression loading, which can be challenging, mainly due to the high fragility and low load-bearing behavior of highly randomized solid skeleton mesh structures [70]. Experimental characteristic compression stress-strain response curves are shown in Fig. 3.23, while the corresponding elastic modulus values $E_{5\%}$, $E_{25\%}$, $E_{50\%}$, $E_{75\%}$ calculated at strain 5 %, 25 %, 50 %, and 75 %, correspondingly, and strength values $\sigma_{50\%}$ calculated at strain 50 % are summarized in Table 3.7. The obtained stress-strain diagrams exhibit three distinct deformation regions – the linear

elastic range, followed by an almost horizontal stress plateau and rapid stress increase range at high strain intensities due to the material's densification [71]. As seen in Table 3.7, the samples measured tensile properties, such as the compressive elastic modulus and strength, increase with density increment [72]. Moreover, Fig. 3.24 (a) and (b) show that the elastic modulus reveals a power-law relationship with its density, and specific strength shows a linear dependence from the NC content. The hemp NFC foam provided a 4-fold higher elastic modulus at an absolute bulk density of 8–9 mg/cc than the wood NFC foam sample (Fig. 3.24 (a)). While Fig. 3.24 (b) reveals a similar tendency observed for the specific strength (σ/ρ), it testified 6-fold higher values for hemp foam compared to the wood foam prepared from 1 wt% NFC suspension. The observation could relate to the complex effect of a more extensive crystallinity index of NC fibrils, the higher length/diameter aspect ratio observed in hemp NFC.

Table 3.7

Physical Properties of the Obtained NC Foams: Bulk Density, Porosity, Compressive Modulus and Strength for Various Strain Levels and Densities

Sample	**Bulk density (mg/cc)**	**Porosity (%)**	$E_{5\%}$ **(kPa)**	$E_{25\%}$ **(kPa)**	$E_{50\%}$ **(kPa)**	$E_{75\%}$ **(kPa)**	$\sigma_{50\%}$ **(kPa)**
Wood NFC							
0.2 wt%	4	99.8	0.17	0.27	0.27	6.61	0.13
0.5 wt%	8	99.5	1.16	0.71	1.32	7.89	0.66
1.0 wt%	14	99.2	2.03	2.01	4.05	22.2	2.02
3.0 wt%	36	97.8	28.2	35.6	52.8	164.6	26.5
Hemp NFC							
0.2 wt%	2	99.9	1.04	0.47	0.36	0.97	0.18
0.5 wt%	6	99.6	2.93	2.63	4.00	10.8	2.04
1.0 wt%	9	99.4	7.59	6.96	10.7	50.5	5.34
3.0 wt%	11	99.3	16.1	16.1	23.1	90.1	11.6

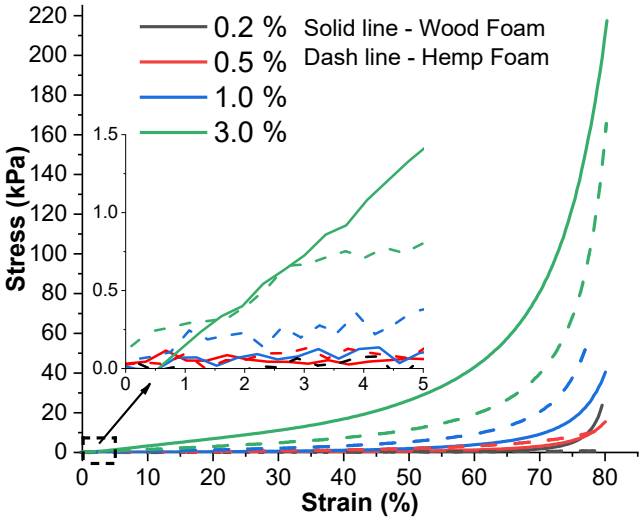

Fig. 3.23. Compressive stress-strain curves of wood and hemp foam samples up to 80 % strain: solid line – wood foams and dash line – hemp foams.

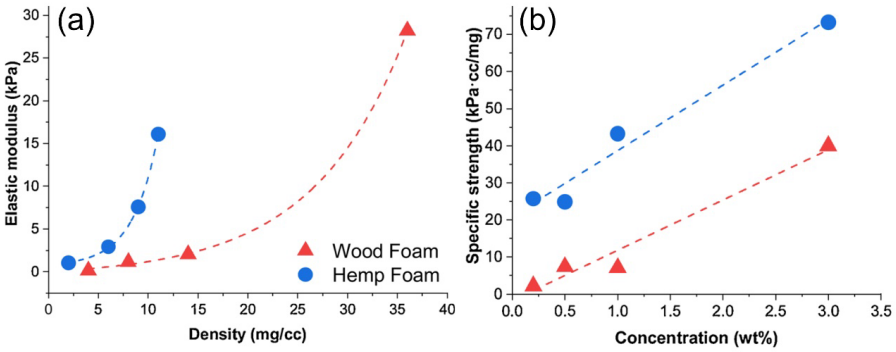

Fig. 3.24. Elastic modulus dependence from foam density (a), specific strength dependence from the suspension concentration (b): red – wood samples; blue – hemp samples.

3.4.6. Thermal conductivity properties

The thermal conductivity of NC foam materials was investigated by the transient plane source method. The experimentally measured effective thermal conductivity of the produced foams as a function of porosity (pore volume fraction) is shown in Fig. 3.25. Thermal conductivity decreases with the increasing porosity of samples. The data for both wood and hemp NFC foams follow the same trend. Error bars for k are comparable with symbol sizes, while data scatter for porosity is more noticeable, particularly for wood NFC foams. The measured values (0.033–0.044 W/m·K) are well in the range of 0.015–0.07 W/m K of other studies on cellulose nanomaterial-based foams [72,73]. The low thermal conductivities could be achieved independently of pore sizes [74].

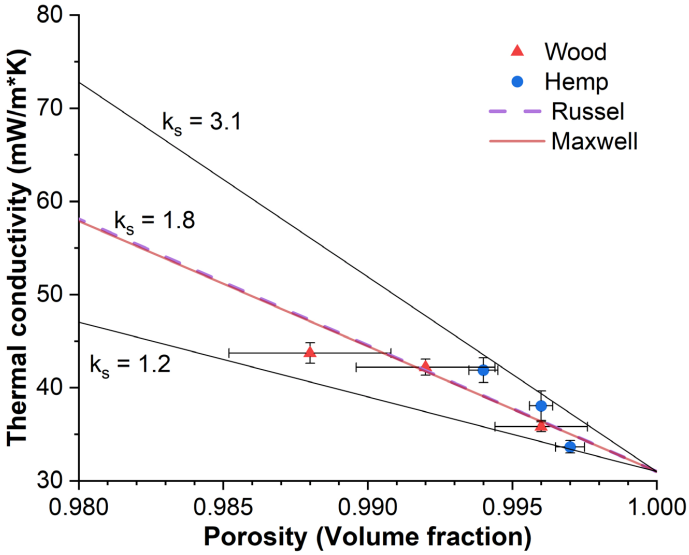

Fig. 3.25. Thermal conductivity of obtained foams as a function of porosity. Symbols represent experimental data; lines represent calculations.

3.4.7. Summary

Birchwood and hemp biomass wastes were used and processed into sustainable NC foam materials. The freeze-drying process can achieve a controlled density between 2 g/cc and 36 g/cc and a porosity of 99.7 % to 99.9 %, resulting in foam materials with enhanced mechanical and thermal insulation properties.

The effect of the NFC content in suspension used for freeze-drying and resulting material density was studied to understand these sustainable foams' compression, thermal degradation, and thermal conductivity. The usage of the hemp NCF for foam preparation strongly enhanced the mechanical properties and thermal conductivity compared to the similar foams obtained from wood NC fibrils, as determined by compression and hot-plate measurements. Thermal degradation analysis showed good thermal stability for both raw and alkaline-treated hemp and wood samples. The elastic modulus reveals a power-law relationship with density increment, and specific strength shows a linear dependence from the cellulose content in suspension used for the freeze-drying process for both types of foams. Accordingly, the thermal conductivity of the obtained NC foams is in the range of 34–44 mW/m·K.

3.5. Sustainable Foams from Hemp, Lignin, Xylan, Pectin, and Glycerol: Tunable via Reversible Citric Acid Crosslinking for Absorption and Insulation Applications (accepted)

3.5.1. Chemical interactions

Figure 3.26 gives insights into the chemical interactions leading to the formation of a crosslinked network for the H- and WM- foams. A detailed investigation of cellulose, xylan, and lignin is provided elsewhere [75-78]. H-foams show strongly pronounced characteristic crosslinking peak changes (Fig. 3.26 (a)), which is reflected in the evident decrease of the broad -OH peak intensity (3040 cm^{-1} to 3600 cm^{-1}) and increase in the carbonyl C=O peak intensity (1733 cm^{-1}) representing formed ester bonds [79]. However, this effect is less pronounced in the spectra of WM-foams due to the much larger amount of -OH bonds introduced by lignin and hemicellulose. The WM-foams spectra in Fig. 3.26 (b) indicate a noticeable shift of the peak assigned to lignin aryl ring stretching (from 1590 cm^{-1} to 1605 cm^{-1}), indicating an electron balance shift caused by the changes of the -OH groups to newly created crosslinks with CA and other components. Due to the substantially lower concentration of lignin, this shift is not pronounced for the H-foams.

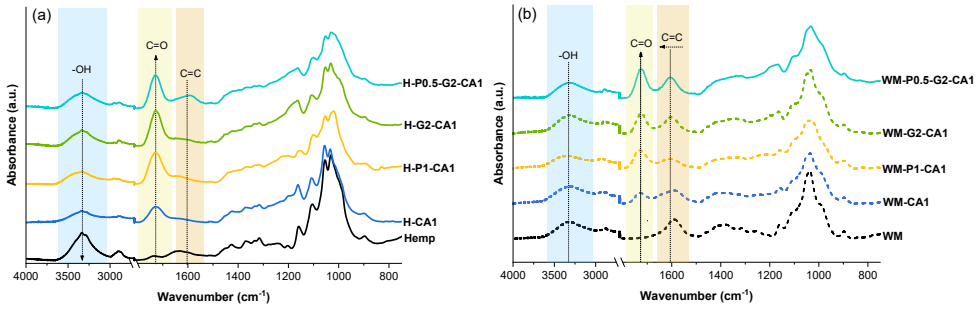

Fig. 3.26. FTIR spectra of selected samples for Hemp foams (a), and WM foams (b).

3.5.2 Morphology

The morphologies of foam samples are shown in Fig. 3.27. NFC forms robust physical gels in aqueous media due to its elongated fiber length, which culminates in an interwoven network characterized by extensive hydrogen bonding. Existing literature demonstrates that the freeze-drying of NFC tends to yield a sheet-like morphology [80,81], a consequence of the aggregation phenomena inherent to NFC.

A coexistence of sheet-like and nanofibrillar structures was observed in the context of H- and WM-foams. Previous analyses indicate that hemp comprises approximately 69 wt% cellulose [61], whereas the WM composition is characterized by about 31 wt% cellulose (45 wt% hemp). This compositional difference is instrumental in defining the mixed structure of the foams. Lower cellulose concentrations (WM-foams) promoted a more pronounced sheet-like structure with increased fiber and sheet thickness.

Incremental increases in the crosslinker (CA) concentration resulted in a morphological transition, introducing micro-sized fiber structures, particularly pronounced in CA5-foams. As

the CA concentration increased, there was a noticeable reduction in nanostructured elements, leading to a decrease in the specific surface area of the foams.

The integration of pectin into the foams induced significant structural transformations. It is noteworthy that the proportion of pectin utilized is substantial, with the NFC and pectin ratio maintained at 6:1 and 3:2 for H-P0.25-CA1 and H-P1-CA1, respectively. Consequently, pectin constitutes a significant portion of the foam's structural network. Pectin achieved an exceptional distribution through a dissolution process, resulting in a nanofibrillar structure with diameters less than 100 nm. These nanofibrillar networks of pectin efficiently occupied the larger pores between cellulosic structures, contributing to a denser and more refined nanostructured network. Glycerol acts as a surface coating for biopolymers, thickening existing structural elements and consequently transforming the foam structure into a microfiber-sized network with diameters predominantly exceeding 1 μm.

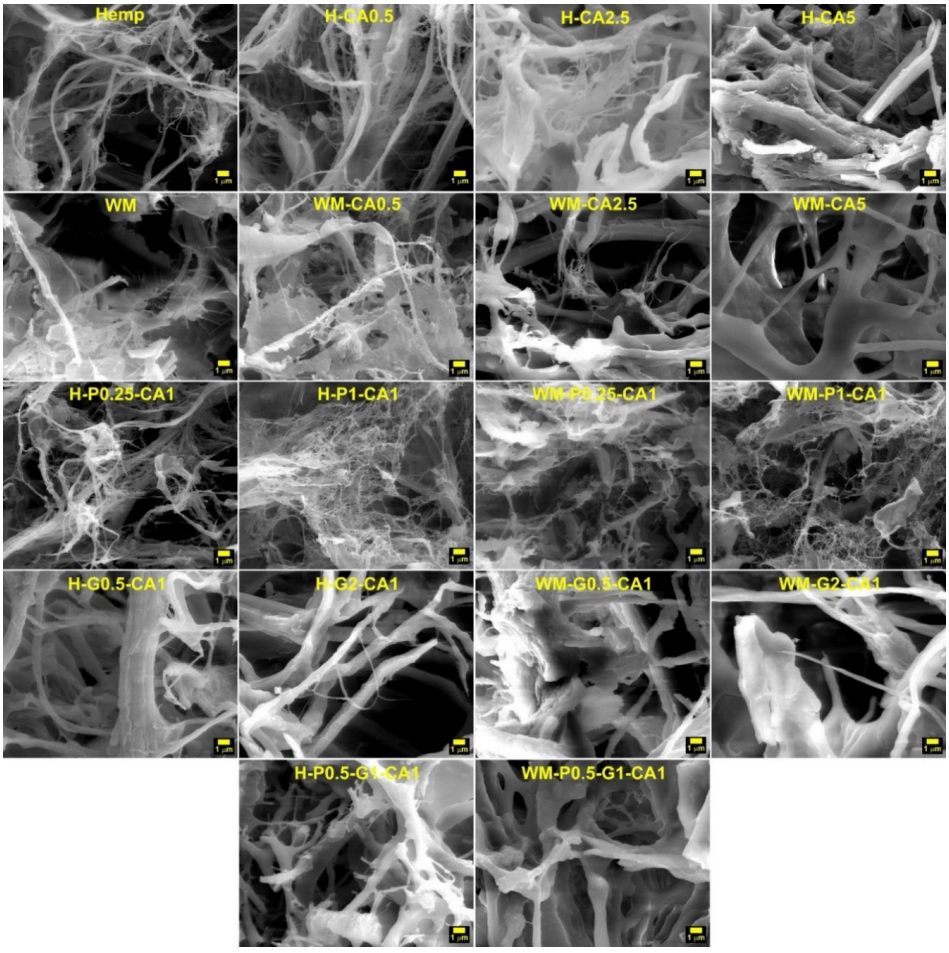

Fig. 3.27. SEM micrographs of selected foam samples shown at 5000× magnification.

3.5.3. Mechanical performance

Figure 3.28 graphically represents the bulk density of the foam samples, with observed values spanning from 13 mg/cm^3 to 152 mg/cm^3. Hemp foam exhibits the lowest bulk density at 13 mg/cc, while WM foam shows a substantial increase, approximately 100 % higher, with a density of 27 mg/cm^3. For hemp foam, the crosslinking process with citric acid (CA) results in a nearly linear increase in density, yet the effect on WM foam exhibits a distinctly non-linear pattern. The incorporation of pectin (P) and glycerol (G) into the H-foam formulation results in an approximate 50 % increase in density. In contrast, the impact on the WM foam structure shows only a marginal increase in density.

Table 3.8 shows that most foam samples exhibit porosity ranging from approximately 97 % to 99 %, underscoring the formation of a highly open and porous structure. These porosity values are in correlation with the observed densities. It is noteworthy that lower porosity values, ranging between 90 % and 94 %, were exhibited in WM-CA5 and the pectin-glycerol hybrid foams.

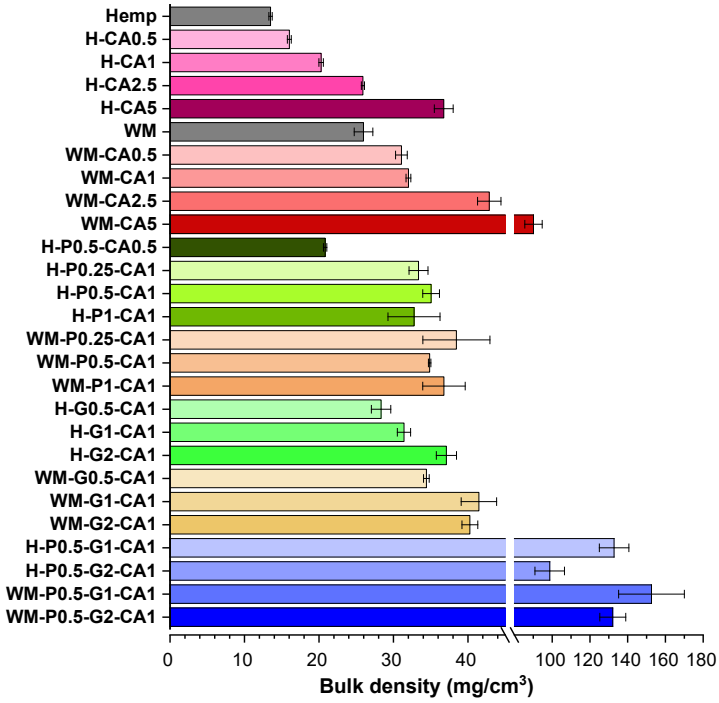

Fig. 3.28. Bulk density of all prepared foam samples.

To investigate the impact of crosslinker citric acid, pectin, and glycerol on the mechanical properties of the foams, a series of compressive stress-strain (σ–ε) tests were conducted. Figure 3.19 depicts the compression curves for foams with varied pectin and glycerol contents. Table 3.8 provides a comprehensive summary of the compressive modulus, specific compressive modulus, and specific strength of these foams. The significant differences in foam density required the use of specific values for comparison. Nearly all compositions adhered to cellulose-

based lightweight materials' typical compression curve profile [82]. During the initial linear phase, stress increased linearly (up to 10 % deformation), indicative of elastic deformation. This was followed by a plateau phase, where stress remained relatively constant, signifying plastic deformation, observable from 15 % to 50 % (and in some cases up to 60 %) deformation. The final phase, densification, was marked by a significant rise in stress as the foam walls compressed tightly against each other beyond 70 % deformation. Notably, hybrid foams with added pectin and glycerol began densification at approximately 60 % deformation.

Table 3.8

Physical Properties of the Obtained Foams: Porosity, Volume Shrinkage, Compressive Modulus, and Specific Strength for Various Strain Levels

Sample	Porosity (%)	Volume shrinkage (%)	$E_{5\%}$ (kPa)	Spec. $E_{5\%}$ (kPa·cm^3/g)	Spec. strength at 5 % strain (kPa·cm^3/g)	Spec. strength at 10 % strain (kPa·cm^3/g)	Spec. strength at 50 % strain (kPa·cm^3/g)
Hemp	99.1 ± 0.01	34.1 ± 1.1	0.096 ± 0.003	7.1 ± 0.2	35.6 ± 1.1	94.9 ± 3.0	709 ± 22
H-CA0.5	98.9 ± 0.02	31.7 ± 0.5	0.109 ± 0.002	6.8 ± 0.1	39.3 ± 0.7	89.7 ± 1.6	749 ± 14
H-CA1	98.6 ± 0.02	42.3 ± 1.8	0.188 ± 0.004	9.3 ± 0.2	70.4 ± 1.5	171 ± 4	1245 ± 26
H-CA2.5	98.3 ± 0.01	35.9 ± 2.4	0.376 ± 0.032	14.5 ± 1.2	139 ± 12	312 ± 27	1727 ± 147
H-CA5	97.5 ± 0.08	37.0 ± 2.4	1.554 ± 0.146	42.3 ± 4.0	576 ± 54	1038 ± 98	2639 ± 248
WM	98.3 ± 0.08	41.6 ± 0.6	0.368 ± 0.042	14.2 ± 1.6	141 ± 16	326 ± 37	1942 ± 222
WM-CA0.5	97.9 ± 0.05	38.0 ± 2.6	0.486 ± 0.058	15.6 ± 1.9	182 ± 21	425 ± 51	3239 ± 387
WM-CA1	97.9 ± 0.02	34.6 ± 0.9	0.982 ± 0.022	30.7 ± 1.7	368 ± 10	738 ± 17	3284 ± 74
WM-CA2.5	97.1 ± 0.11	39.7 ± 2.1	1.515 ± 0.335	35.3 ± 7.8	567 ± 125	1282 ± 284	4592 ± 1015
WM-CA5	94.0 ± 0.31	64.4 ± 1.2	4.559 ± 1.035	50.6 ± 11.5	1716 ± 389	3780 ± 858	11585 ± 2630
H-P0.5-CA0.5	98.6 ± 0.01	33.7 ± 0.6	1.136 ± 0.124	54.5 ± 5.9	422 ± 46	897 ± 98	2928 ± 320
H-P0.25-CA1	97.8 ± 0.08	52.6 ± 2.1	1.372 ± 0.245	41.1 ± 7.3	514 ± 92	1060 ± 189	3817 ± 682
H-P0.5-CA1	97.7 ± 0.07	58.8 ± 2.6	1.556 ± 0.232	44.4 ± 6.6	577 ± 86	1297 ± 193	4603 ± 686
H-P1-CA1	97.8 ± 0.23	44.5 ± 4.5	2.138 ± 0.473	65.3 ± 14.4	793 ± 175	1794 ± 397	6056 ± 1340
WM-P0.25-CA1	97.4 ± 0.30	43.9 ± 5.1	2.060 ± 0.134	53.6 ± 3.5	764 ± 49	1594 ± 104	5248 ± 341
WM-P0.5-CA1	97.7 ± 0.01	35.5 ± 2.8	2.938 ± 0.126	84.3 ± 3.6	1089 ± 46	2113 ± 91	5707 ± 245
WM-P1-CA1	97.5 ± 0.19	33.5 ± 4.1	5.796 ± 0.652	157.6 ± 17.7	2165 ± 243	4981 ± 560	10822 ± 1217
H-G0.5-CA1	98.1 ± 0.09	41.4 ± 5.0	0.237 ± 0.003	8.4 ± 0.1	87.5 ± 4.1	245 ± 3	1475 ± 19
H-G1-CA1	97.9 ± 0.07	36.0 ± 4.0	0.407 ± 0.024	13.0 ± 0.8	151 ± 10	385 ± 23	1883 ± 111
H-G2-CA1	97.5 ± 0.09	34.7 ± 2.4	0.569 ± 0.031	15.3 ± 0.8	212 ± 12	465 ± 25	2520 ± 137
WM-G0.5-CA1	97.7 ± 0.03	32.5 ± 1.0	0.504 ± 0.055	14.6 ± 1.6	187 ± 20	378 ± 41	2239 ± 244
WM-G1-CA1	97.2 ± 0.16	38.2 ± 6.1	0.593 ± 0.073	14.3 ± 1.8	211 ± 26	497 ± 61	2224 ± 274
WM-G2-CA1	97.3 ± 0.07	42.1 ± 3.0	0.777 ± 0.092	19.3 ± 2.3	290 ± 34	575 ± 68	3269 ± 387
H-P0.5-G1-CA1	91.1 ± 0.52	81.7 ± 1.3	24.800 ± 4.342	186.7 ± 32.7	9191 ± 1609	14306 ± 2505	56926 ± 9967
H-P0.5-G2-CA1	93.4 ± 0.52	75.5 ± 2.3	20.000 ± 3.457	202.6 ± 35.0	7412 ± 1281	16307 ± 2819	43540 ± 7526
WM-P0.5-G1-CA1	89.8 ± 1.16	81.6 ± 2.1	46.600 ± 7.762	305.4 ± 50.9	17270 ± 2876	42028 ± 7000	110443 ± 18396
WM-P0.5-G2-CA1	91.2 ± 0.46	79.0 ± 0.6	30.200 ± 5.213	228.6 ± 39.5	11192 ± 1932	26091 ± 4504	74123 ± 12795

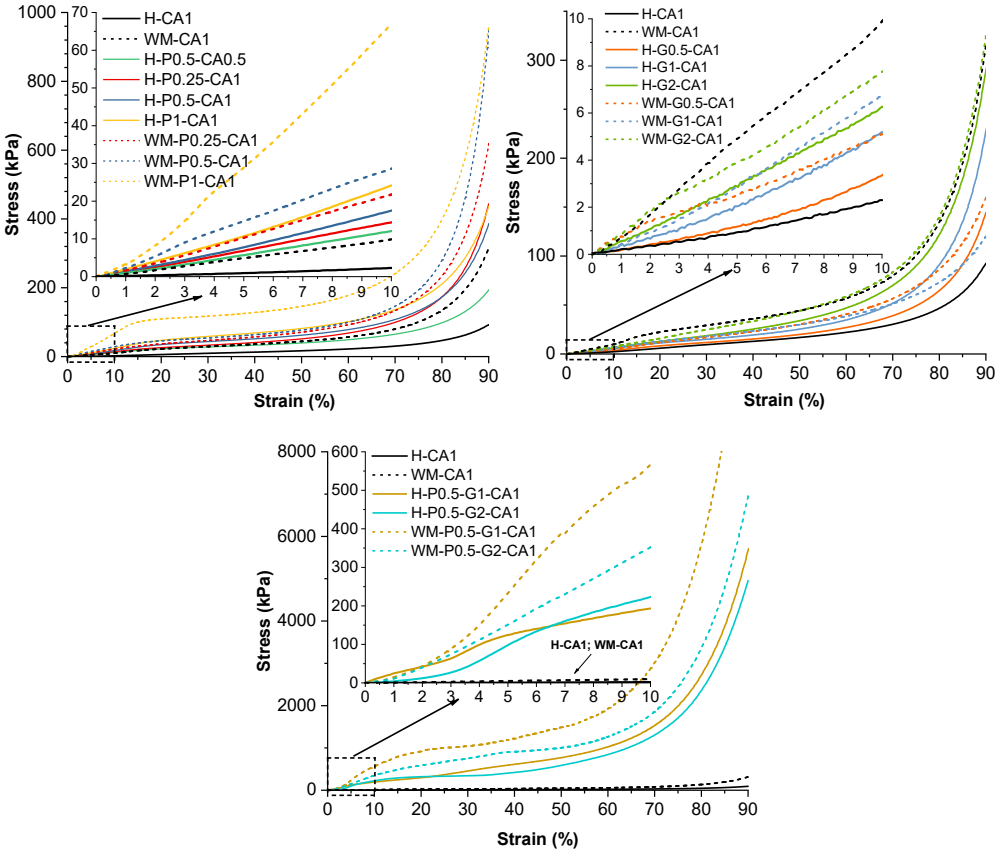

Fig. 3.29. Compression curves for foams with varied pectin and glycerol contents.

3.5.4. Absorption characterization

Investigating the behavior of ultralight, low-density foams in aqueous environments is crucial for their application in pollution removal from water. Their efficiency in this regard depends on a comprehensive understanding of their interaction with both hydrophobic and hydrophilic substances. In Fig. 3.30, water contact angle measurements are presented. All foams were tested without any surface processing, and the contact angle values were examined after 10 s and 60 s. As a result, hydrophilic and hydrophobic foam surfaces can be distinguished.

The base composition analysis reveals that WM-foams demonstrate a pronounced affinity for water, contrasting with H-foams, which exhibit an initial contact angle of approximately 130° across varying concentrations of crosslinking agent CA. Notably, H-CA0.5 foams show a substantial decrease in contact angle over time. With a high concentration of CA, WM-foams approach the hydrophobic characteristics of H-foams, albeit with a gradual water absorption leading to a significant decrease in contact angle after 60 s. The hydrophilic nature of WM-foams is attributed to the presence of xylan, a smaller molecule than cellulose, capable of

forming robust physical crosslinks with cellulose fibrils and filling structural voids. This likely increases surface hydroxyl groups, a tendency that higher CA concentrations can moderate.

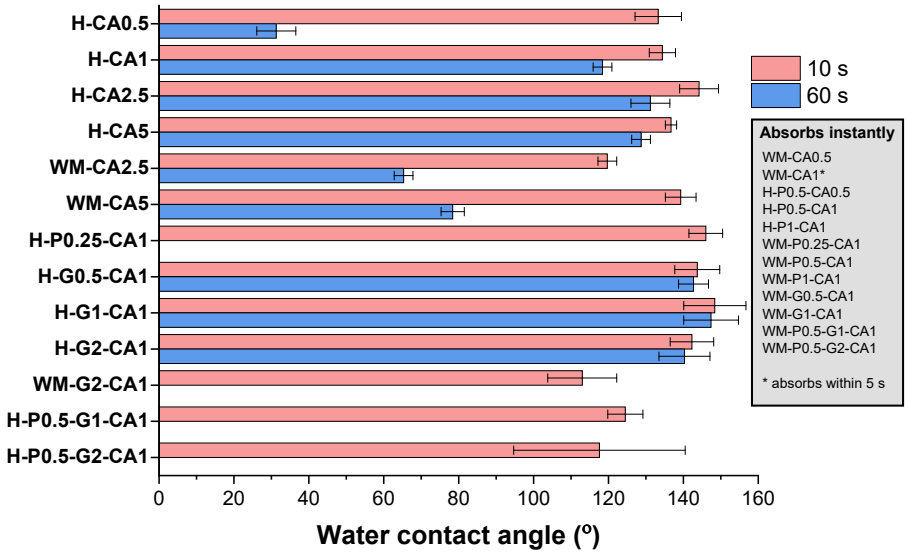

Fig. 3.30. Foam water contact angle measurements.

Figure 3.31 illustrates the differential absorption capacity and selectivity of various foam compositions towards three distinct liquids: water, rapeseed oil, and kerosene (a medium-chain hydrocarbon derived from petroleum distillation). This distinction is crucial as water absorption pertains to the removal of dyes and heavy metals. In contrast, rapeseed oil and kerosene are representative of viscous organic liquids and liquid fuel spills, respectively. Notably, certain foam formulations exhibited pronounced hydrophobicity, resisting water absorption. However, it was discovered that mechanical compression could induce absorption in these hydrophobic foams.

3.5.5. Thermal conductivity

Table 3.9 presents the thermal conductivity, diffusivity, and specific heat of various foam compositions to evaluate their insulation application potential. The highlight of foams is their hydrophobic performance, suggesting their viability as long-term stable thermal insulators. The thermal conductivity of these foams ranges from 0.040 W/m·K to 0.046 W/m·K, which aligns them with materials like industrial polyurethane foam [83], wool [84], and other high-performance insulation materials [85]. Notably, these values are about 2-fold higher than the best-reported figures for cellulose aerogels [31], reflecting morphological distinctions between foams and aerogels. Intriguingly, foam density showed no significant correlation with thermal conductivity. The thermal diffusivity and specific heat measurements align with expected performance parameters, including their error margins.

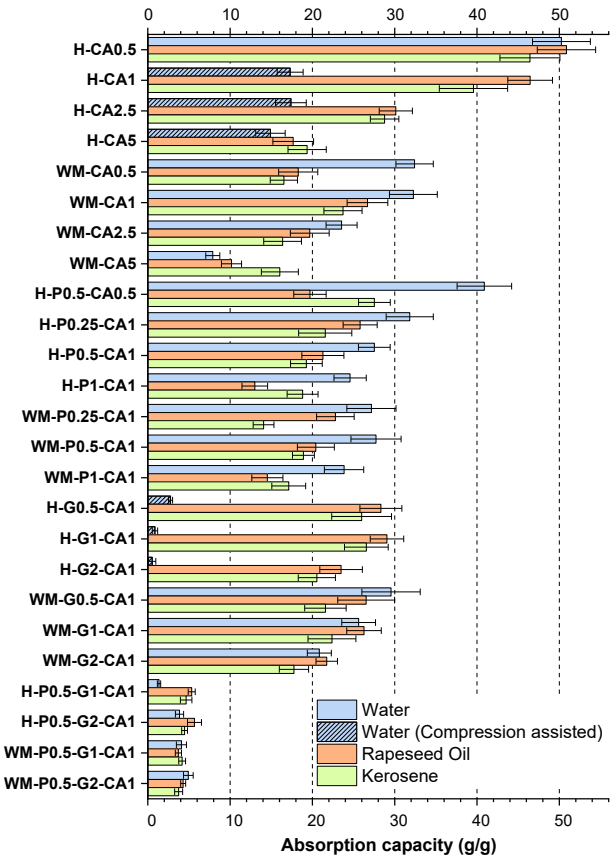

Fig. 3.31. Absorption capacity of foam samples in water, rapeseed oil and kerosene.

Table 3.9

Thermal Conductivity, Diffusivity, and Specific Heat of Various Foam Compositions

Sample	Th. conductivity (W/m·K)	Th. diffusivity (mm^2/s)	Specific heat (MJ/m^3K)
Hemp	0.044 ± 0.001	0.91 ± 0.17	0.050 ± 0.011
H-CA1	0.041 ± 0.001	0.97 ± 0.19	0.044 ± 0.011
H-CA2.5	0.040 ± 0.000	0.80 ± 0.13	0.052 ± 0.010
WM	0.044 ± 0.001	0.74 ± 0.19	0.064 ± 0.018
WM-CA1	0.045 ± 0.001	0.73 ± 0.16	0.065 ± 0.014
WM-CA2.5	0.045 ± 0.001	1.16 ± 0.23	0.041 ± 0.010
H-P0.25-CA1	0.046 ± 0.002	0.80 ± 0.25	0.063 ± 0.019
H-P1-CA1	0.045 ± 0.001	0.69 ± 0.13	0.068 ± 0.013
WM-P0.25-CA1	0.044 ± 0.002	1.28 ± 0.28	0.036 ± 0.008
WM-P1-CA1	0.044 ± 0.002	0.60 ± 0.16	0.079 ± 0.021
H-G0.5-CA1	0.040 ± 0.001	0.77 ± 0.20	0.055 ± 0.014
H-G2-CA1	0.046 ± 0.002	0.40 ± 0.10	0.124 ± 0.033
WM-G0.5-CA1	0.041 ± 0.001	0.68 ± 0.16	0.063 ± 0.013
WM-G2-CA1	0.045 ± 0.001	0.89 ± 0.20	0.054 ± 0.017

3.5.6. Summary

The study demonstrates the preparation of multifunctional foams with highly tunable properties based on composition. Biobased, biocompatible, and renewable components were selected as the basis for the preparation of thermally crosslinked foams. The investigated properties relate to applications such as insulation, filtration, and environmental cleanup, while areas such as biomedical and sound dampening are applicable but were not explored in this study. Based on the experimental results, the following conclusions are presented:

1. FTIR spectroscopy confirms the formation of a crosslinked hybrid network around hemp fibrils characterized by the formation of ester bonds, particularly pronounced in H-foam spectra.
2. H- and WM-foams exhibit structures ranging from sheet-like to nanofibrillar. Pectin creates a dense network of nanofibrillar structures below 100 nm, while glycerol transforms the structure into a microfiber network with diameters predominantly above 1 µm. The bulk density of foams varies from 13 mg/cm^3 to 152 mg/cm^3, with H-based ones being the least dense. Porosity values range from 97 % to 99 %, decreasing to 90–93 % in certain hybrid foams.
3. The specific compressive modulus and specific strength significantly increase with higher CA concentrations. A 10-fold increase in CA concentration results in a 6-fold increase in specific modulus and a 16-fold increase in specific strength (at 5 % strain) for H-foams. Pectin improves specific modulus up to 9-fold and specific strength up to 22-fold at 5 % strain in H-foams.
4. H-CA0.5 demonstrated the highest absorption capacity for water (50 g/g), rapeseed oil (51 g/g), and kerosene (46 g/g). Pectin integration enhances rapid absorption across all liquids, while glycerol increases hydrophobicity, stabilizing water contact angles between 140° and 150° for H-G-foams.
5. The thermal conductivity of the foam ranges from 0.040 W/m·K to 0.046 W/m·K, positioning them as viable thermal insulators, especially highly hydrophobic foams.
6. Pectin and glycerol hybrid foams demonstrated exceptional rigidity and mechanical performance, but their structure and shrinkage also limited their potential in the examined application scenarios.

CONCLUSIONS

1. The advanced extraction and manipulation of lignocellulose from diverse biomass sources, including wood pulp, wood dust, and agricultural hemp residues, and its combination with externally sourced hemicellulose and lignin can create bioplastics and foams that mimic the structural and mechanical properties of natural wood.

2. The integration of hybrid modifiers, such as lignin and xylan, into the structure of nanofibrillated cellulose significantly enhances the performance of cellulose nanopapers and foams. The structure can be regulated by fine-tuning the content of lignin and xylan and by utilizing green chemical functionalization and crosslinking approaches.

3. Through the mechanical processing of hemp stalks and subsequent thermal crosslinking using natural additives, it is possible to develop sustainable bioplastics whose properties range from brittle to ductile (elastic modulus 913–2927 MPa) by systematically adjusting the varying ratios of xylan, citric acid and other components, highlighting the possibility of creating customizable, eco-friendly materials suitable for various applications.

4. Creating eco-friendly nanolignocellulose foams from wood dust and hemp stalk waste yields lightweight materials with customizable mechanical strength ($E_{5\%}$ 0.17–28.2 kPa), porosity (97.8–99.9 %), and thermal insulation (0.033–0.044 W/m·K). Fine-tuning the nanofibril content allows for tailored properties to meet specific industry needs, while environmentally friendly functionalization methods enable the creation of foams with adjustable properties spanning from soft to rigid (spec. $E_{5\%}$ 6.8–305.4 kPa·cm^3/g). These versatile foams find applications in thermal insulation, filtration systems, environmental cleanup, and more.

5. Cellulose nanopapers display varying degrees of resilience to environmental stressors such as UV radiation, heat, and humidity, with UV-Vis and FTIR spectroscopy revealing that while lignin and xylan components undergo degradation, the core cellulose fibers maintain their structural integrity, demonstrating the potential for cellulose-based plastics in environmentally sensitive applications.

6. The resulting wood mimic materials exhibit a notable array of properties, including high tensile strength, stiffness, thermal stability, and biodegradability. Moreover, they can be tailored to meet specific application requirements, such as packaging materials, construction components, and sorption or separation materials. Furthermore, the sustainable nature of these materials aligns with the principles of the circular economy. By harnessing the abundant resources of cellulose, hemicellulose, and lignin, this Thesis represents a step forward in the development of environmentally friendly biomaterials, potentially fostering a greener and more sustainable future.

REFERENCES

1. Rosenboom, J.-G.; Langer, R.; Traverso, G. Bioplastics for a circular economy. *Nature Reviews Materials* **2022**, *7*, 117-137, doi:10.1038/s41578-021-00407-8.
2. Dziuba, R.; Kucharska, M.; Madej-Kiełbik, L.; Sulak, K.; Wiśniewska-Wrona, M. Biopolymers and Biomaterials for Special Applications within the Context of the Circular Economy. *Materials (Basel)* **2021**, *14*, doi:10.3390/ma14247704.
3. Rana, A.K.; Guleria, S.; Gupta, V.K.; Thakur, V.K. Cellulosic pine needles-based biorefinery for a circular bioeconomy. *Bioresource Technology* **2023**, *367*, 128255, doi:https://doi.org/10.1016/j.biortech.2022.128255.
4. Geyer, R.; Jambeck, J.R.; Law, K.L. Production, use, and fate of all plastics ever made. *Science Advances* **2017**, *3*, e1700782, doi:doi:10.1126/sciadv.1700782.
5. Pan, X.; Li, J.; Ma, N.; Ma, X.; Gao, M. Bacterial cellulose hydrogel for sensors. *Chemical Engineering Journal* **2023**, *461*, 142062, doi:https://doi.org/10.1016/j.cej.2023.142062.
6. Lan, Z.; Wang, Y.; Hu, K.; Shi, S.; Meng, Q.; Sun, Q.; Shen, X. Anti-swellable cellulose hydrogel for underwater sensing. *Carbohydrate Polymers* **2023**, *306*, 120541, doi:https://doi.org/10.1016/j.carbpol.2023.120541.
7. Han, X.; Ding, S.; Zhu, L.; Wang, S. Preparation and characterization of flame-retardant and thermal insulating bio-based composite aerogels. *Energy and Buildings* **2023**, *278*, 112656, doi:https://doi.org/10.1016/j.enbuild.2022.112656.
8. Wang, Y.; Yang, J.; Song, Y.; Yang, Q.; Xiong, C.; Shi, Z. Porous and three-dimensional carbon aerogels from nanocellulose/pristine graphene for high-performance supercapacitor electrodes. *Diamond and Related Materials* **2023**, *132*, 109626, doi:https://doi.org/10.1016/j.diamond.2022.109626.
9. Jamróz, E.; Kulawik, P.; Kopel, P. The Effect of Nanofillers on the Functional Properties of Biopolymer-Based Films: A Review. *Polymers* **2019**, *11*, 675.
10. Tyuftin, A.A.; Kerry, J.P. Gelatin films: Study review of barrier properties and implications for future studies employing biopolymer films. *Food Packaging and Shelf Life* **2021**, *29*, 100688, doi:https://doi.org/10.1016/j.fpsl.2021.100688.
11. Temesgen, S.; Rennert, M.; Tesfaye, T.; Nase, M. Review on Spinning of Biopolymer Fibers from Starch. *Polymers* **2021**, *13*, 1121.
12. Gough, C.R.; Rivera-Galletti, A.; Cowan, D.A.; Salas-de la Cruz, D.; Hu, X. Protein and Polysaccharide-Based Fiber Materials Generated from Ionic Liquids: A Review. *Molecules* **2020**, *25*, 3362.
13. Song, B.; Lin, R.; Lam, C.H.; Wu, H.; Tsui, T.-H.; Yu, Y. Recent advances and challenges of inter-disciplinary biomass valorization by integrating hydrothermal and biological techniques. *Renewable and Sustainable Energy Reviews* **2021**, *135*, 110370, doi:https://doi.org/10.1016/j.rser.2020.110370.
14. Burla, F.; Mulla, Y.; Vos, B.E.; Aufderhorst-Roberts, A.; Koenderink, G.H. From mechanical resilience to active material properties in biopolymer networks. *Nature Reviews Physics* **2019**, *1*, 249-263, doi:10.1038/s42254-019-0036-4.
15. Gregory, D.A.; Tripathi, L.; Fricker, A.T.R.; Asare, E.; Orlando, I.; Raghavendran, V.; Roy, I. Bacterial cellulose: A smart biomaterial with diverse applications. *Materials Science and Engineering: R: Reports* **2021**, *145*, 100623, doi:https://doi.org/10.1016/j.mser.2021.100623.
16. Noremylia, M.B.; Hassan, M.Z.; Ismail, Z. Recent advancement in isolation, processing, characterization and applications of emerging nanocellulose: A review.

International Journal of Biological Macromolecules **2022**, *206*, 954-976, doi:https://doi.org/10.1016/j.ijbiomac.2022.03.064.
17. Feng, P.; He, J.; Peng, S.; Gao, C.; Zhao, Z.; Xiong, S.; Shuai, C. Characterizations and interfacial reinforcement mechanisms of multicomponent biopolymer based scaffold. *Materials Science and Engineering: C* **2019**, *100*, 809-825, doi:https://doi.org/10.1016/j.msec.2019.03.030.
18. Pei, Y.; Wang, L.; Tang, K.; Kaplan, D.L. Biopolymer Nanoscale Assemblies as Building Blocks for New Materials: A Review. *Advanced Functional Materials* **2021**, *31*, 2008552, doi:https://doi.org/10.1002/adfm.202008552.
19. Jin, H.; Zha, C.; Gu, L. Direct dissolution of cellulose in NaOH/thiourea/urea aqueous solution. *Carbohydrate Research* **2007**, *342*, 851-858, doi:https://doi.org/10.1016/j.carres.2006.12.023.
20. Fauziyah, M.a.; Widiyastuti, W.; Balgis, R.; Setyawan, H. Production of cellulose aerogels from coir fibers via an alkali–urea method for sorption applications. *Cellulose* **2019**, *26*, 9583-9598, doi:10.1007/s10570-019-02753-x.
21. Budtova, T. Cellulose II aerogels: a review. *Cellulose* **2019**, *26*, 81-121, doi:10.1007/s10570-018-2189-1.
22. Mohd, N.; Draman, S.F.S.; Salleh, M.S.N.; Yusof, N.B. Dissolution of cellulose in ionic liquid: A review. *AIP Conference Proceedings* **2017**, *1809*, doi:10.1063/1.4975450.
23. Verma, C.; Mishra, A.; Chauhan, S.; Verma, P.; Srivastava, V.; Quraishi, M.A.; Ebenso, E.E. Dissolution of cellulose in ionic liquids and their mixed cosolvents: A review. *Sustainable Chemistry and Pharmacy* **2019**, *13*, 100162, doi:https://doi.org/10.1016/j.scp.2019.100162.
24. Chen, Y.-L.; Zhang, X.; You, T.-T.; Xu, F. Deep eutectic solvents (DESs) for cellulose dissolution: a mini-review. *Cellulose* **2019**, *26*, 205-213, doi:10.1007/s10570-018-2130-7.
25. Budtova, T.; Aguilera, D.A.; Beluns, S.; Berglund, L.; Chartier, C.; Espinosa, E.; Gaidukovs, S.; Klimek-kopyra, A.; Kmita, A.; Lachowicz, D.; et al. Biorefinery approach for aerogels. *Polymers* **2020**, *12*, 1-63, doi:10.3390/polym12122779.
26. Klein, M.; Poverenov, E. Natural biopolymer-based hydrogels for use in food and agriculture. *Journal of the Science of Food and Agriculture* **2020**, *100*, 2337-2347, doi:https://doi.org/10.1002/jsfa.10274.
27. Ahmed, E.M. Hydrogel: Preparation, characterization, and applications: A review. *Journal of Advanced Research* **2015**, *6*, 105-121, doi:https://doi.org/10.1016/j.jare.2013.07.006.
28. Cascone, S.; Lamberti, G. Hydrogel-based commercial products for biomedical applications: A review. *International Journal of Pharmaceutics* **2020**, *573*, 118803, doi:https://doi.org/10.1016/j.ijpharm.2019.118803.
29. Wei, G.; Zhang, J.; Usuelli, M.; Zhang, X.; Liu, B.; Mezzenga, R. Biomass vs inorganic and plastic-based aerogels: Structural design, functional tailoring, resource-efficient applications and sustainability analysis. *Progress in Materials Science* **2022**, *125*, 100915, doi:https://doi.org/10.1016/j.pmatsci.2021.100915.
30. García-González, C.A.; Sosnik, A.; Kalmár, J.; De Marco, I.; Erkey, C.; Concheiro, A.; Alvarez-Lorenzo, C. Aerogels in drug delivery: From design to application. *Journal of Controlled Release* **2021**, *332*, 40-63, doi:https://doi.org/10.1016/j.jconrel.2021.02.012.
31. Chen, Y.; Zhang, L.; Yang, Y.; Pang, B.; Xu, W.; Duan, G.; Jiang, S.; Zhang, K. Recent Progress on Nanocellulose Aerogels: Preparation, Modification, Composite

Fabrication, Applications. *Advanced Materials* **2021**, *33*, 2005569, doi:https://doi.org/10.1002/adma.202005569.
32. Poursorkhabi, V.; Abdelwahab, M.A.; Misra, M.; Khalil, H.; Gharabaghi, B.; Mohanty, A.K. Processing, Carbonization, and Characterization of Lignin Based Electrospun Carbon Fibers: A Review. *Frontiers in Energy Research* **2020**, *8*, doi:10.3389/fenrg.2020.00208.
33. Khalid, M.Y.; Arif, Z.U. Novel biopolymer-based sustainable composites for food packaging applications: A narrative review. *Food Packaging and Shelf Life* **2022**, *33*, 100892, doi:https://doi.org/10.1016/j.fpsl.2022.100892.
34. Cui, C.; Fu, Q.; Meng, L.; Hao, S.; Dai, R.; Yang, J. Recent Progress in Natural Biopolymers Conductive Hydrogels for Flexible Wearable Sensors and Energy Devices: Materials, Structures, and Performance. *ACS Applied Bio Materials* **2021**, *4*, 85-121, doi:10.1021/acsabm.0c00807.
35. Van Vlierberghe, S.; Dubruel, P.; Schacht, E. Biopolymer-Based Hydrogels As Scaffolds for Tissue Engineering Applications: A Review. *Biomacromolecules* **2011**, *12*, 1387-1408, doi:10.1021/bm200083n.
36. Reddy, M.S.B.; Ponnamma, D.; Choudhary, R.; Sadasivuni, K.K. A Comparative Review of Natural and Synthetic Biopolymer Composite Scaffolds. *Polymers* **2021**, *13*, 1105.
37. Ambekar, R.S.; Kandasubramanian, B. Progress in the Advancement of Porous Biopolymer Scaffold: Tissue Engineering Application. *Industrial & Engineering Chemistry Research* **2019**, *58*, 6163-6194, doi:10.1021/acs.iecr.8b05334.
38. Chatterjee, S.; Hui, P.C.-l. Review of Applications and Future Prospects of Stimuli-Responsive Hydrogel Based on Thermo-Responsive Biopolymers in Drug Delivery Systems. *Polymers* **2021**, *13*, 2086.
39. Hasnain, M.S.; Ahmed, S.A.; Alkahtani, S.; Milivojevic, M.; Kandar, C.C.; Dhara, A.K.; Nayak, A.K. Biopolymers for Drug Delivery. In *Advanced Biopolymeric Systems for Drug Delivery*, Nayak, A.K., Hasnain, M.S., Eds.; Springer International Publishing: Cham, 2020; pp. 1-29.
40. Segal, L.; Creely, J.J.; Martin, A.E.; Conrad, C.M. An Empirical Method for Estimating the Degree of Crystallinity of Native Cellulose Using the X-Ray Diffractometer. *Textile Research Journal* **1959**, *29*, 786-794, doi:10.1177/004051755902901003.
41. Leung, A.C.W.; Lam, E.; Chong, J.; Hrapovic, S.; Luong, J.H.T. Reinforced plastics and aerogels by nanocrystalline cellulose. *Journal of Nanoparticle Research* **2013**, *15*, doi:10.1007/s11051-013-1636-z.
42. Hubbe, M.A.; Tayeb, P.; Joyce, M.; Tyagi, P.; Kehoe, M.; Dimic-Misic, K.; Pal, L. Rheology of Nanocellulose-rich Aqueous Suspensions: A Review. *2017* **2017**, *12*, 106.
43. Auzins, J.; Janushevskis, A.; Janushevskis, J.; Skukis, E. Software EDAOpt for experimental design, analysis and multiobjective robust optimization. *OPT-i 2014 - 1st International Conference on Engineering and Applied Sciences Optimization, Proceedings* **2014**, 1055-1077.
44. Zhang, N.; Tao, P.; Lu, Y.; Nie, S. Effect of lignin on the thermal stability of cellulose nanofibrils produced from bagasse pulp. *Cellulose* **2019**, *26*, 7823-7835, doi:10.1007/s10570-019-02657-w.
45. I.P., M.; B., W.; Tamrin; H., I.; J.A., M. Thermal and Morphology Properties of Cellulose Nanofiber from TEMPO-oxidized Lower part of Empty Fruit Bunches (LEFB). *Open Chemistry* **2019**, *17*, 526-536, doi:doi:10.1515/chem-2019-0063.

46. Shen, D.; Zhang, L.; Xue, J.; Guan, S.; Liu, Q.; Xiao, R. Thermal degradation of xylan-based hemicellulose under oxidative atmosphere. *Carbohydr Polym* **2015**, *127*, 363-371, doi:10.1016/j.carbpol.2015.03.067.
47. Uetani, K.; Hatori, K. Thermal conductivity analysis and applications of nanocellulose materials. *Science and Technology of Advanced Materials* **2017**, *18*, 877-892, doi:10.1080/14686996.2017.1390692.
48. Diaz, J.A.; Ye, Z.; Wu, X.; Moore, A.L.; Moon, R.J.; Martini, A.; Boday, D.J.; Youngblood, J.P. Thermal Conductivity in Nanostructured Films: From Single Cellulose Nanocrystals to Bulk Films. *Biomacromolecules* **2014**, *15*, 4096-4101, doi:10.1021/bm501131a.
49. Gaidukovs, S.; Zukulis, E.; Bochkov, I.; Vaivodiss, R.; Gaidukova, G. Enhanced mechanical, conductivity, and dielectric characteristics of ethylene vinyl acetate copolymer composite filled with carbon nanotubes. *Journal of Thermoplastic Composite Materials* **2018**, *31*, 1161-1180, doi:10.1177/0892705717734603.
50. Bertasius, P.; Macutkevic, J.; Banys, J.; Gaidukovs, S.; Barkane, A.; Vaivodiss, R. Synergy effects in dielectric and thermal properties of layered ethylene vinyl acetate composites with carbon and Fe3O4 nanoparticles. *Journal of Applied Polymer Science* **2020**, *137*, 48814, doi:https://doi.org/10.1002/app.48814.
51. Desai, R.L.; Shields, J.A. Photochemical degradation of cellulose material. *Die Makromolekulare Chemie* **1969**, *122*, 134-144, doi:https://doi.org/10.1002/macp.1969.021220111.
52. Łojewski, T.; Miśkowiec, P.; Missori, M.; Lubańska, A.; Proniewicz, L.M.; Łojewska, J. FTIR and UV/vis as methods for evaluation of oxidative degradation of model paper: DFT approach for carbonyl vibrations. *Carbohydrate Polymers* **2010**, *82*, 370-375, doi:https://doi.org/10.1016/j.carbpol.2010.04.087.
53. Zięba-Palus, J.; Trzcińska, B.; Weselucha-Birczyńska, A.; Moskal, P.; Sacharz, J. The sequence of changes observed during degradation process of paper by the use of UV/VIS and FTIR spectrometry with application of the PCA and 2D correlation method for forensic purposes. *Journal of Molecular Structure* **2020**, *1205*, 127651, doi:https://doi.org/10.1016/j.molstruc.2019.127651.
54. Liu, J.; Chinga-Carrasco, G.; Cheng, F.; Xu, W.; Willför, S.; Syverud, K.; Xu, C. Hemicellulose-reinforced nanocellulose hydrogels for wound healing application. *Cellulose* **2016**, *23*, 3129-3143, doi:10.1007/s10570-016-1038-3.
55. Tedeschi, G.; Guzman-Puyol, S.; Ceseracciu, L.; Paul, U.C.; Picone, P.; Di Carlo, M.; Athanassiou, A.; Heredia-Guerrero, J.A. Multifunctional Bioplastics Inspired by Wood Composition: Effect of Hydrolyzed Lignin Addition to Xylan–Cellulose Matrices. *Biomacromolecules* **2020**, *21*, 910-920, doi:10.1021/acs.biomac.9b01569.
56. Goksu, E.I.; Karamanlioglu, M.; Bakir, U.; Yilmaz, L.; Yilmazer, U. Production and Characterization of Films from Cotton Stalk Xylan. *Journal of Agricultural and Food Chemistry* **2007**, *55*, 10685-10691, doi:10.1021/jf071893i.
57. Liu, Y.; Hu, T.; Wu, Z.; Zeng, G.; Huang, D.; Shen, Y.; He, X.; Lai, M.; He, Y. Study on biodegradation process of lignin by FTIR and DSC. *Environmental Science and Pollution Research* **2014**, *21*, 14004-14013, doi:10.1007/s11356-014-3342-5.
58. Ebringerová, A.; Novotná, Z.; Kačuráková, M.; Machová, E. Chemical modification of beechwood xylan with p-carboxybenzyl bromide. *Journal of Applied Polymer Science* **1996**, *62*, 1043-1047, doi:https://doi.org/10.1002/(SICI)1097-4628(19961114)62:7<1043::AID-APP10>3.0.CO;2-7.
59. Abidi, N.; Cabrales, L.; Haigler, C.H. Changes in the cell wall and cellulose content of developing cotton fibers investigated by FTIR spectroscopy. *Carbohydrate Polymers* **2014**, *100*, 9-16, doi:https://doi.org/10.1016/j.carbpol.2013.01.074.

60. Cogulet, A.; Blanchet, P.; Landry, V. Wood degradation under UV irradiation: A lignin characterization. *Journal of Photochemistry and Photobiology B: Biology* **2016**, *158*, 184-191, doi:https://doi.org/10.1016/j.jphotobiol.2016.02.030.
61. Beluns, S.; Gaidukovs, S.; Platnieks, O.; Gaidukova, G.; Mierina, I.; Grase, L.; Starkova, O.; Brazdausks, P.; Thakur, V.K. From Wood and Hemp Biomass Wastes to Sustainable Nanocellulose Foams. *Industrial Crops and Products* **2021**, *170*, 113780, doi:https://doi.org/10.1016/j.indcrop.2021.113780.
62. Rana, R.; Langenfeld-Heyser, R.; Finkeldey, R.; Polle, A. FTIR spectroscopy, chemical and histochemical characterisation of wood and lignin of five tropical timber wood species of the family of Dipterocarpaceae. *Wood Science and Technology* **2010**, *44*, 225-242, doi:10.1007/s00226-009-0281-2.
63. Beluns, S.; Gaidukovs, S.; Platnieks, O.; Barkane, A.; Gaidukova, G.; Grase, L.; Nabels-Sneiders, M.; Kovalovs, A.; Thakur, V.K. Clean manufacturing of cellulose nanopapers by incorporating lignin and xylan as sustainable additives. *Carbohydrate Polymer Technologies and Applications* **2022**, *3*, doi:10.1016/j.carpta.2022.100207.
64. Branca, C.; Di Blasi, C. Kinetic assessment of the thermal decomposition of hemp fiber and the impact of pretreatments. *Journal of Thermal Analysis and Calorimetry* **2022**, doi:10.1007/s10973-022-11663-3.
65. Li, J.; Liu, Y.; Sun, B.; Zhang, R. Improving the wet strength of hemicelluloses based composite films by citric acid crosslinking. *Journal of Wood Chemistry and Technology* **2021**, *41*, 1-9, doi:10.1080/02773813.2020.1847147.
66. Kargarzadeh, H.; Ahmad, I.; Abdullah, I.; Dufresne, A.; Zainudin, S.Y.; Sheltami, R.M. Effects of hydrolysis conditions on the morphology, crystallinity, and thermal stability of cellulose nanocrystals extracted from kenaf bast fibers. *Cellulose* **2012**, *19*, 855-866, doi:10.1007/s10570-012-9684-6.
67. Foster, E.J.; Moon, R.J.; Agarwal, U.P.; Bortner, M.J.; Bras, J.; Camarero-Espinosa, S.; Chan, K.J.; Clift, M.J.D.; Cranston, E.D.; Eichhorn, S.J.; et al. Current characterization methods for cellulose nanomaterials. *Chemical Society Reviews* **2018**, *47*, 2609-2679, doi:10.1039/C6CS00895J.
68. Rahbar Shamskar, K.; Heidari, H.; Rashidi, A. Preparation and evaluation of nanocrystalline cellulose aerogels from raw cotton and cotton stalk. *Industrial Crops and Products* **2016**, *93*, 203-211, doi:10.1016/j.indcrop.2016.01.044.
69. Platnieks, O.; Gaidukovs, S.; Barkane, A.; Sereda, A.; Gaidukova, G.; Grase, L.; Thakur, V.K.; Filipova, I.; Fridrihsone, V.; Skute, M.; et al. Bio-based poly(butylene succinate)/microcrystalline cellulose/nanofibrillated cellulose-based sustainable polymer composites: Thermo-mechanical and biodegradation studies. *Polymers* **2020**, *12*, 1-20, doi:10.3390/polym12071472.
70. Rege, A.; Schestakow, M.; Karadagli, I.; Ratke, L.; Itskov, M. Micro-mechanical modelling of cellulose aerogels from molten salt hydrates. *Soft Matter* **2016**, *12*, 7079-7088, doi:10.1039/c6sm01460g.
71. Han, J.; Yue, Y.; Wu, Q.; Huang, C.; Pan, H.; Zhan, X.; Mei, C.; Xu, X. Effects of nanocellulose on the structure and properties of poly(vinyl alcohol)-borax hybrid foams. *Cellulose* **2017**, *24*, 4433-4448, doi:10.1007/s10570-017-1409-4.
72. Gupta, P.; Singh, B.; Agrawal, A.K.; Maji, P.K. Low density and high strength nanofibrillated cellulose aerogel for thermal insulation application. *Materials & Design* **2018**, *158*, 224-236, doi:10.1016/j.matdes.2018.08.031.
73. Apostolopoulou-Kalkavoura, V.; Munier, P.; Bergström, L. Thermally Insulating Nanocellulose-Based Materials. *Advanced Materials n/a*, 2001839, doi:https://doi.org/10.1002/adma.202001839.

74. Long, L.Y.; Weng, Y.X.; Wang, Y.Z. Cellulose Aerogels: Synthesis, Applications, and Prospects. *Polymers (Basel)* **2018**, *10*, doi:10.3390/polym10060623.
75. Javier-Astete, R.; Jimenez-Davalos, J.; Zolla, G. Determination of hemicellulose, cellulose, holocellulose and lignin content using FTIR in Calycophyllum spruceanum (Benth.) K. Schum. and Guazuma crinita Lam. *PLOS ONE* **2021**, *16*, e0256559, doi:10.1371/journal.pone.0256559.
76. Beluns, S.; Platnieks, O.; Gaidukovs, S.; Starkova, O.; Sabalina, A.; Grase, L.; Thakur, V.K.; Gaidukova, G. Lignin and Xylan as interface engineering additives for improved environmental durability of sustainable cellulose nanopapers. *International Journal of Molecular Sciences* **2021**, *22*, doi:10.3390/ijms222312939.
77. Chen, Z.; Hu, T.Q.; Jang, H.F.; Grant, E. Modification of xylan in alkaline treated bleached hardwood kraft pulps as classified by attenuated total-internal-reflection (ATR) FTIR spectroscopy. *Carbohydrate Polymers* **2015**, *127*, 418-426, doi:https://doi.org/10.1016/j.carbpol.2015.03.084.
78. Derkacheva, O.; Sukhov, D. Investigation of Lignins by FTIR Spectroscopy. *Macromolecular Symposia* **2008**, *265*, 61-68, doi:https://doi.org/10.1002/masy.200850507.
79. Beluns, S.; Gaidukovs, S.; Platnieks, O.; Grase, L.; Gaidukova, G.; Thakur, V.K. Sustainable hemp-based bioplastics with tunable properties via reversible thermal crosslinking of cellulose. *International Journal of Biological Macromolecules* **2023**, *242*, 125055, doi:https://doi.org/10.1016/j.ijbiomac.2023.125055.
80. Ali, Z.M.; Gibson, L.J. The structure and mechanics of nanofibrillar cellulose foams. *Soft Matter* **2013**, *9*, 1580-1588, doi:10.1039/C2SM27197D.
81. Lavoine, N.; Bergström, L. Nanocellulose-based foams and aerogels: processing, properties, and applications. *Journal of Materials Chemistry A* **2017**, *5*, 16105-16117, doi:10.1039/c7ta02807e.
82. Ferreira, E.S.; Rezende, C.A.; Cranston, E.D. Fundamentals of cellulose lightweight materials: bio-based assemblies with tailored properties. *Green Chemistry* **2021**, *23*, 3542-3568, doi:10.1039/D1GC00326G.
83. Schiavoni, S.; D'Alessandro, F.; Bianchi, F.; Asdrubali, F. Insulation materials for the building sector: A review and comparative analysis. *Renewable and Sustainable Energy Reviews* **2016**, *62*, 988-1011, doi:https://doi.org/10.1016/j.rser.2016.05.045.
84. Abu-Jdayil, B.; Mourad, A.-H.; Hittini, W.; Hassan, M.; Hameedi, S. Traditional, state-of-the-art and renewable thermal building insulation materials: An overview. *Construction and Building Materials* **2019**, *214*, 709-735, doi:https://doi.org/10.1016/j.conbuildmat.2019.04.102.
85. Kumar, D.; Alam, M.; Zou, P.X.W.; Sanjayan, J.G.; Memon, R.A. Comparative analysis of building insulation material properties and performance. *Renewable and Sustainable Energy Reviews* **2020**, *131*, 110038, doi:https://doi.org/10.1016/j.rser.2020.110038.

Sergejs Beļuns was born in 1992 in Valmiera. He obtained a Bachelor's degree in Chemical Technology (2015) and a Master's degree in Materials Science (2017) from Riga Technical University (RTU). He was a technologist at "Polipaks" Ltd. Since 2020, he has been a scientific assistant and researcher at Riga Technical University. Currently, he is a researcher at the Institute of Chemistry and Chemical Technology. His scientific interests are related to the extraction and research of cellulosic bioplastics.